A MODELING STUDY OF LOCAL SURFACE HETEROGENEITIES AND THEIR IMPACT ON WETTING AND ADHESION BEHAVIOR IN DRY AND HUMID ENVIRONMENTS

A Dissertation

Presented to the Faculty of the Graduate School

of Cornell University

in Partial Fulfillment of the Requirements for the Degree of

Doctor of Philosophy

by

Elizabeth Savoy

May 2014

A MODELING STUDY OF LOCAL SURFACE HETEROGENEITIES AND THEIR IMPACT ON WETTING AND ADHESION BEHAVIOR IN DRY AND HUMID ENVIRONMENTS

Elizabeth Savoy, Ph.D.

Cornell University 2014

Surfaces may appear to be flat and homogeneous by human observation, but upon closer inspection at sub-micron length scales they can reveal a rich and quite varied chemistry and topology which impart sometimes unexpected behaviors, such as the self-cleaning lotus leaf, or insects which can walk on water. There exist many theoretical equations which often provide reliable estimates of macroscopic properties such as surface energy, fluid contact angle, or individual forces contributing to adhesion between surfaces. However, because many of these theories rely on assumptions about ideal geometry and chemical homogeneity, they may not accurately capture the details of wetting and adhesive behavior at sub-micron length scales. For applications which rely on nanoscale features, such as micro-fluidics, chemically active laboratory or consumer product surfaces, or understanding how the aforementioned biological systems work, those local heterogeneities are key to understanding and manipulating interfacial behavior.

By applying molecular dynamics simulations to ideal mesoscopic surfaces with features designed to prevent wetting, and atomistic amorphous surfaces in various environments, we studied interfacial behavior for systems of interest. Using rare-event sampling techniques we quantified the thermodynamics and kinetics of the wetting transition to show that re-entrant roughness features can be constructed to increase the transition energy barrier for moderately phillic fluids, but as the in-

trinsic contact angle of that fluid decreases, representing a decrease in fluid surface tension, the chemistry quickly dominates the free energy landscape, resulting in full wetting of the idealized surface despite the topological transition energy barrier. The wetting transition state is shown to depend on fluctuations in the fluid interface, a condition which is not considered in most macroscopic treatments. At the atomistic level, we performed adhesion energy simulations on an amorphous glass surface in dry and humid conditions. Our results indicate that the type of surface hydroxyl can impact how strongly the surface will adhere to another similar surface, depending on both potential of interaction and steric factors within the bulk. Specifically, addition of B-hydroxyl groups reduces the adhesion between surfaces as compared to a pure silica surface. Additionally, conditions of low relative humidity show lower adhesion than high humidity, as a liquid bridge is unable to form below about 10% RH.

Interfacial behavior of solid surfaces at the sub-micron scale is a result of complex interplay between local chemistry and topology, which change the functional response of those surfaces in ways that may not be predicted by macroscale equations. Molecular simulations can elucidate the impact of local conditions and lead to methods for controlling surface performance.

BIOGRAPHICAL SKETCH

Elizabeth was born in Bellefonte, Pennsylvania, and grew up in Manheim and Lewistown, Pennsylvania. She completed two years in Chemical Engineering at Bucknell University, lived in Germany for years, then finished her undergraduate degree in Chemical Engineering at Auburn University in Alabama. She began working at Corning Incorporated in 1995 in the Process Engineering and Modeling group, where she learned to apply programming to industrial and research problems, including heat transfer modeling of hot glass forming processes, thermal and stress modeling of plastic injection molding, and heat and mass transfer modeling of ceramic substrates. For several years she led a team of developers to build internal optical network modeling tools, and established procedures for best programming practices within her department, focusing on lean solutions. In 2007 she entered the PhD program in the School of Chemical and Biomolecular Engineering at Cornell University, while remaining an employee of Corning Incorporated. Under the guidance of Professor Fernando Escobedo she applied molecular dynamics transition path sampling techniques to study the wetting of rough surfaces, and adhesion between surfaces in dry and humid environments. Elizabeth plans to continue her career at Corning Incorporated in the Modeling and Simulation department, working on molecular modeling of materials, with emphasis on understanding interfacial phenomena. She has been married for 24 years to Chris Savoy, and has three children, Claudia (16), Gretchen (15) and Matthew (13). She is also an avid distance runner.

This document is dedicated to my father, Donald Earl Evans, and my mother, JoAnn Fae Stewart Schopf Evans.

ACKNOWLEDGEMENTS

I would like to thank many people at Corning Incorporated and Cornell University for helping me on my journey. Dipak Chowdhury and Les Button, for the initial encouragement and support to get started on this path. Professor Paulette Clancy for believing in me from the get-go and showing me that this was an achievable goal, and that Cornell was the right place to do it. Professors Fernando Escobedo, Abe Stroock, Brad Anton, Lynden Archer and Roger Loring for their utterly inspirational ways of teaching difficult material. My colleagues at Corning: Gautam Meda, Amy Rovelstad, Les Button, Jim Rustad, Deena Vargheese, Adama Tandia, and M K Badrinarayan, for sustained support and encouragement and many invaluable technical discussions. My project leaders, Adra Baca and Wanda Walczak, for working with me to find areas of interest that would fit with my thesis research and understanding my constraints. The NIC guys at Corning who maintain an amazingly robust and powerful computational borg which was essentially my laboratory: Joe, Steve, Matt, Matt, Chris, Charles, and Jim. And for the dedicated lengthy efforts required to work through the legal and logistical issues for me to remain an employee at Corning while pursuing a degree at Cornell: Ron Snyder, Gautam Meda, Professor Paulette Clancy and Dean Ellen Gainor. To Shelby Clark-Shevalier and Barbara Edinger for answering my endless administrative questions. My group members at various times at Cornell: Umang, Camilo, Bernardo, Francisco, Pooja, Poornima, Stacey, Carlos, Salomon, Sushmit, Mihir and Vikram for being ever encouraging, inspiring and fun to be around. My special committee, Professors Susan Daniel and Roger Loring from Cornell, and Dr. Adra Baca from Corning Incorporated. And my advisor, Professor Fernando Escobedo, for encouraging me to join the Chemical Engineering graduate program at Cornell; for inspiring me to want to, and figure out how to, understand statistical thermo-

dynamics; for his patience, support, technical input to my work, sense of humor and fantastic attitude.

Also, I am eternally grateful to my family and friends whose support has been instrumental in my success. My parents, Don and JoAnn Evans, who in addition to instilling in me the belief that I can do anything I set my mind to, also have been heavily involved in the day-to-day business of raising my three children, making it possible for me to work and go to school. Claudia, Gretchen and Matthew, who have grown from small children to very likable young adults throughout my graduate school experience, and who always understand when I need time for schoolwork. To know that they are proud of me means the world. My husband, Chris Savoy, who has been there to pick up the slack at home, encouraging, supportive and understanding of the stresses related to being a mom, working and being in school. To my good friends who always have an ear, good advice, and wouldn't let me consider giving up: Melissa, Zaga, Zora, and many others. And to my community of running friends and teams, my outlet for stepping away from the responsibilities of school and work for a bit, and where I learn to Finish Strong and just be.

TABLE OF CONTENTS

LIST OF TABLES

LIST OF FIGURES

CHAPTER 1

MOLECULAR SIMULATIONS OF WETTING OF A ROUGH SURFACE BY AN OILY FLUID: EFFECT OF TOPOLOGY, CHEMISTRY AND DROPLET SIZE ON WETTING TRANSITION RATES*

1.1 Abstract

The goal of this work is to study via molecular simulations the wetting kinetics of a rough surface by an oily fluid. We use Forward Flux Sampling to compute the wetting transition rate and elucidate the transition mechanism of a small droplet on a surface of nails. The nails provide the re-entrant geometry necessary to keep the droplet in the non-wetted, composite state. The effects of nail height, droplet size, and surface chemistry are investigated. Since the droplet must touch the bottom surface in order to transition, increasing the nail height is an effective way to increase the barrier to wetting for both phobic and slightly phillic drops, although as the fluid becomes very phillic chemistry dominates and the effect of nail height disappears. Generally smaller drops transition more easily. Overall, our results suggest that non-wettability could be practically enhanced by promoting the "kinetic" trapping of the system in the non-wetted state.

* Reprinted with permission from Escobedo, F. A.; *Langmuir* **2012**, *28*, 3412-3419.

1.2 Introduction

Design of surface topology and chemistry to promote desired wetting behavior continues to be of interest for applications such as microfluidic systems, anti-biofouling, biosensing, heat exchange and self-cleaning surfaces [32]. Recent advancements in fabrication techniques make nanoscale feature design realizable [21, 24]. Water's high surface tension and polarity make superhydrophobic surfaces readily achievable, but it remains difficult to make a surface non-wetting to low-surface tension fluids such as oils since these fluids prefer to be in the fully wetted state. Some researchers [28, 27, 16, 20] have succeeded in creating such surfaces, but additional practical constraints such as transparency, durability and manufacturability require alternate solutions. Gaining a better understanding of the interplay between chemistry and topology, and identifying the most significant factors to promote non-wetting, remain an important endeavor and are the goals of the current research.

Wettability of a surface is determined by its chemistry and topology, as well as the chemistry of the fluid. Young's equation [34], $\cos\theta^Y = (\gamma_{SV} - \gamma_{SL})/\gamma_{LV}$, shows the effect of chemistry (solid, liquid and vapor interfacial energies, γ) on the intrinsic contact angle, θ^Y. The well known Wenzel [33], $\cos\theta^W = r\cos\theta^Y$, and Cassie Baxter [7], $\cos\theta^{CB} = -1 + \phi_s[\cos\theta^Y + 1]$, equations account for the effect of roughness and predict two locally metastable wetting states, where the one with the lower contact angle, θ, is the more stable [25]. (r is the roughness ratio and ϕ_s is fraction of solid in contact with fluid). Setting $\theta^{CB} = \theta^W$ gives a critical intrinsic contact angle, $\theta_C^Y = (\phi_s - 1)/(r - \phi_s)$, above which the non-wetting Cassie-Baxter (composite) state will be the more stable. Since $r > 1 > \phi_s$, then necessarily $\theta_C^Y > 90^o$. In order for a low surface tension fluid to have $\theta^Y > 90$,

the surface energy (γ_{SV}) must be lower than any surface that has been observed or created [28]. Therefore the wetted state, as predicted by the Wenzel equation, will always be preferred by low surface-tension fluids meaning some barrier must be present to maintain the metastable composite state.

One approach to create such a free energy barrier is to use surface roughness with re-entrant geometry [10, 23] such that the fluid must create more surface area in order to advance further into the surface structure. We aim to identify the most significant aspects of the surface roughness to maximize that energy barrier and prevent wetting. 1.1 illustrates our strategy. Although a detailed simulation study of the thermodynamics of this process is still under way (e.g., to precisely estimate ΔG and ΔG^*), our preliminary data indicates that for the slightly phillic chemistry (the main target of this study) the wetted states correspond to the lowest free energy minima (i.e., ΔG in 1.1 is $O(10^2)$ $k_B T$, based on initial Boxed Molecular Dynamics (BXD) [14] runs). The working hypothesis is then that a suitable choice of surface roughness will not significantly alter the thermodynamics (i.e., ΔG) but will increase the kinetic barrier ΔG^* to delay the wetting process enough to make the surface effectively phobic for periods of practical significance (i.e. $\approx$ hours). In this context, it is the rate of the process of primary concern here and the focus of this report.

While continuum models based on Gibbs free energy analysis [25, 22] can be used to estimate the transition energy barrier, the assumption of a flat fluid-vapor interface limits their ability to quantify the transition energy barrier [29]. Koishi et. al. [18] estimated ΔG^* for (phobic) water droplets on pillars using molecular dynamics to study nanodroplet "raining", where the probability of transitioning to the wetted state at different impact velocities was used to find ΔG^* on the order

of 0.1 to 1 kT. Application of this same technique to our system resulted in similar values for ΔG^*, despite the fact that the re-entrant geometry should give much higher free energy barriers. This points to the need for more rigorous evaluation of the free energy barriers of these systems (work currently in progress) and of wetting rates.

Here we use Forward Flux Sampling (FFS) to compute the wetting transition rates and mechanisms for an oily fluid on a model surface of nails, a system which we expect to have a high ΔG^* due to the re-entrant geometry of the nails. FFS is used because the transitions from the composite to the wetted state are "rare events" [9] (note that $\Delta G^* \approx 20\ k_B T$, based on initial BXD [14] runs); i.e., such transitions in our case have time constants in the order of hours and would hence be impossible to study via "brute-force" molecular dynamic runs. We look at the effect of system size, nail height and chemistry. Overall, our results suggest that non-wettability could be practically enhanced by promoting the "kinetic" trapping of the system in the non-wetted state.

1.3 Simulation system

Molecular dynamics simulations were done using the constant volume and temperature NVT ensemble in LAMMPS [26]. The system consists of a cylindrical droplet made up of tetramers of Lennard-Jones (LJ) particles, sitting on a surface of nails. 1.1 shows the system in both low energy basins, the composite and wetted state.

The surface is a flat 2 σ thick slab on the bottom, with nails protruding. The nail posts underneath are 1σ in diameter, and the plates on top are $5 \times 5\sigma^2$ squares

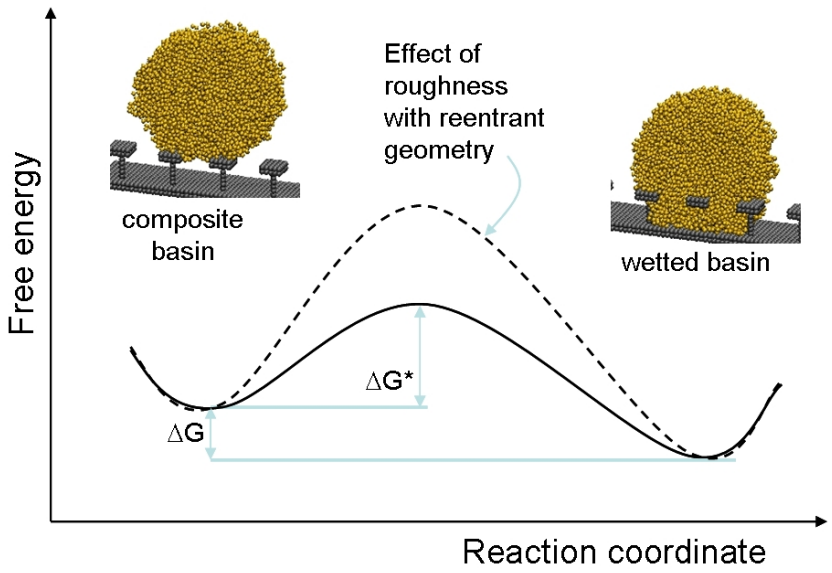

Figure 1.1: Schematics of wetting process going from (left) Cassie-Baxter (composite) non-wetting state to (right) Wenzel, wetting state

and 2σ thick. They are spaced evenly at a distance of 12 and 13 σ between nail posts in the x and z directions, respectively, giving a constant surface fraction of $\phi_s = 0.16$. Note that the y dimension is normal to the surface. Two nail heights are used: 9σ for the "short" nails and 15σ for the "tall" nails. All surface particles are laid out on a simple cubic lattice with 1σ spacing. Surface particles are fixed by not applying time integration to them.

The overall simulation box size is fixed for all drop sizes at $60 \times 40 \times 13\sigma^3$. Periodic boundary conditions are used in the x and z dimensions, and the y dimension is fixed with a reflecting potential at the top of the box above the drop.

The droplet is initially created by choosing random positions within a rectangular box of depth z=13 σ at a density of $\approx$ 1 bead / σ^3, with tetramer bond lengths $\approx 1\sigma$, and random bond angles. A space of a few σ is allowed in the x and y directions around the drop edges, and the constant volume and energy NVE ensemble with a max step of 0.1 σ per particle is applied to relax overlapping par-

ticle positions. The drop is then equilibrated using the NVT ensemble, taking on a cylindrical shape. This drop is placed within 1 σ of the surface of interest and allowed to equilibrate further to take on the truncated cylinder shape as determined by the intrinsic wetting parameter, ϵ_{12}.

The interactions between particles within the fluid are defined by the LJ cut and shifted potential:

$$E = 4\epsilon\left[\left(\frac{\sigma}{r}\right)^{12} - \left(\frac{\sigma}{r}\right)^{6}\right] - 4\epsilon\left[\left(\frac{\sigma}{r_c}\right)^{12} - \left(\frac{\sigma}{r_c}\right)^{6}\right], r < r_c \tag{1.1}$$

with $\epsilon = \sigma = 1.0$, and bonds are described by the FENE [19] potential:

$$E = -0.5KR_0^2 \ln\left[1 - \left(\frac{r}{R_0}\right)^2\right] + 4\epsilon\left[\left(\frac{\sigma}{r}\right)^{12} - \left(\frac{\sigma}{r}\right)^{6}\right] + \epsilon \tag{1.2}$$

with parameters set to maintain a bond length of 1σ ($K = 30\epsilon/\sigma^2, R_0 = 1.5\sigma$). All parameters are defined in LJ units (e.g., $r^* = r/\sigma, T^* = Tk_B/\epsilon$; see Ref. [11]). Based on the properties of tridecane (a representative alkane), $\epsilon = 4.24 \times 10^{-21}$ J, $\sigma = 0.42$ nm, $r_c = 3\sigma$, and $\tau = 1.8$ ps (see Appendix for details on unit evaluation).

Interactions between the fluid and surface also use the LJ potential, with $\sigma = 1.0$, and the intrinsic wetting behavior is determined by the well depth parameter, ϵ_{12}. A series of simulations of static droplets on a flat surface (two layers of simple cubic wall particles) was done to relate ϵ_{12} to the intrinsic contact angle, θ^Y. This calibration is shown in 1.2 for two different size droplets.

Using the NVT ensemble, with $T^* = 1.0$ ($T = \epsilon/k_B = 307$ K), a Langevin thermostat was used to introduce stochasticity (a feature needed by the Forward Flux sampling method described later). The timestep ($0.005\tau \approx 9$ fs) and damping parameter (damp = 20 τ) for the Langevin thermostat were set based on achieving the same bulk diffusion and contact angle vs. ϵ_{12} behavior as when using the Nosé-Hoover thermostat.

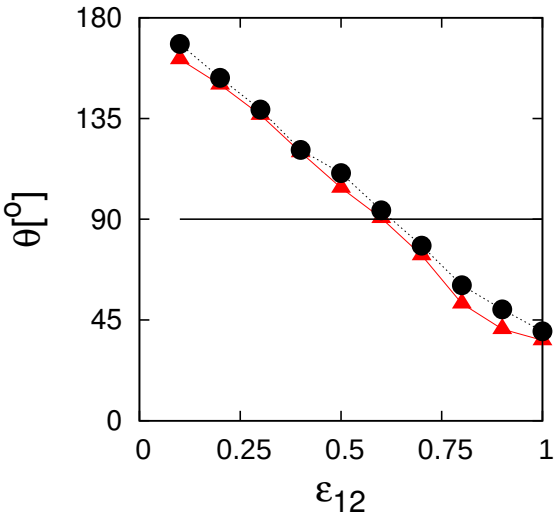

Figure 1.2: Calibration of ϵ_{12} and intrinsic wetting behavior. Nominal droplet diameters for $\theta = 90^o$ are 48σ and 125σ for the 16,000 (red triangles) and 120,000 (black circles) particle droplets, respectively.

For computational efficiency, droplets are represented by a short cylinder of depth 13σ (see 1.1) rather than a hemisphere. The depth of the cylinder was chosen to be larger than the length of a fully extended tetramer plus r_c, and also to allow for uniform nail spacing in both x and y dimensions. Initial simulations on a flat surface comparing contact angle for this system to a fully spherical droplet showed good agreement. It is expected that some deviations will occur when roughness is introduced, but we believe there is sufficient similarity to learn about the thermodynamics and kinetics of the wetting transition.

Several system sizes are studied. Fluid droplet sizes are 2000, 4000, 6000 and 8000 particles ($\approx$ 5-15 nm diameter; for reference, the nail spacing is 5 nm). Snapshots of each are shown in the composite and wetted state on the short nails in 1.3.

Primarily two intrinsic chemistries are used, one which is slightly phobic and one slightly phillic. Several runs were also done with a more phillic chemistry. The

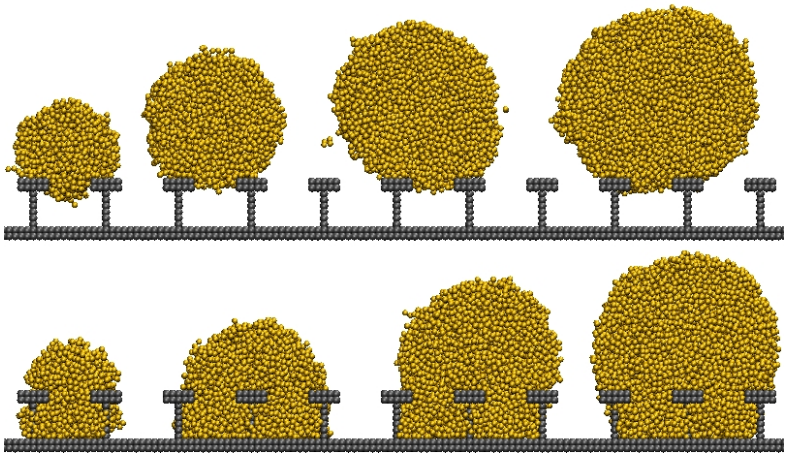

Figure 1.3: Four droplet sizes: 2000, 4000, 6000, 8000 particles from left to right. Shown on short nails, in energy basin A (composite, top) and B (wetted, bottom).

Referred to as	ϵ_{12}	$\theta^Y[^o]$	$\Delta G[k_BT]\dagger$
(slightly) phobic	0.5	105	$\approx$10
(slightly) phillic	0.7	75	O(10^2)
more phillic	0.8	60	$\gg$ O(10^2)
$\dagger$ ΔG values are initial estimates from BXD simulations.			

Table 1.1: Intrinsic Chemistries

values are shown in 1.1. Recall that the intrinsic chemistry is determined by the value of ϵ_{12}, which is the well depth in the Lennard Jones potential between the droplet particles and the surface particles.

To check the validity of the model and establish a relationship to the macroscale, several independent MD simulations were performed to compute a static contact angle on simple square posts of varying height: (2,4,8,12) σ. A larger (16,000 particles) phobic drop was used because the contact angle can be more precisely computed and there are several posts under the drop. 1.4 shows good agreement between simulated contact angles and what is predicted by the macroscopic Wenzel and Cassie-Baxter equations, where the theoretical prediction is the lower of θ^W and θ^{CB}. More importantly, the simulated drop is in the wetted state on the 2 and 4 σ posts, and the composite state on the 8 and 12 σ posts, as predicted by

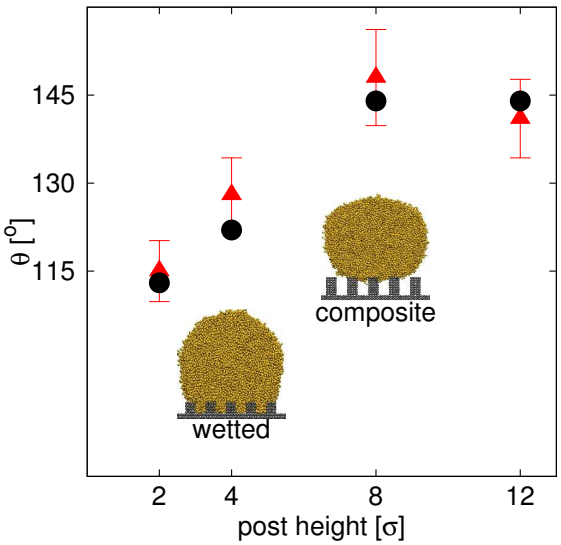

Figure 1.4: Phobic drop on 4×4 σ^2 square posts. As predicted, drop crosses over from wetted (shown on 4 σ high posts) to composite state (shown on 8 σ high posts) with increase in post height. Red triangles: simulated data; Black circles: macroscopic theoretical predictions.

the macroscopic equations. Because the transition point is captured accurately, the small droplet simulations can provide insight to the dynamics of the wetting transition.

Note that the simulated drop on the 4 σ posts was initially stuck in a metastable state where the contact angle was higher. We have found this to be an issue with drops in the wetted state due to the relative size of the drop to roughness features. These states correspond to real local energy minima which are generally not observable experimentally [17]. In this case the drop was forced to spread and wet the next feature by temporarily increasing ϵ_{12}. Care is required when searching for the equilibrium state for drops in the wetted state. Some preliminary simulations (not reported here) indicate that Generalized Hamiltonian Replica Exchange [12] can identify the low energy state. This will be a topic of a future report. For the study of composite to wetted transition, the main focus of this report, metastable states are not an issue.

1.4 Forward Flux Sampling (FFS)

1.4.1 Overview

FFS is a transition path sampling technique that is used to estimate the transition rate from one low energy basin (A) to another (B). The system is systematically ratcheted through the transition state, along an order parameter (λ), while capturing information about the transition kinetics and mechanism. The technique captures true dynamical pathways and does not require prior knowledge of the transition state [2]. The algorithm can be used with MC or stochastic MD; we use the latter in this study. FFS has been used to study the kinetics of different types of transitions (like order-disorder and conformational transitions [6, 30, 3]) but, to the best of our knowledge, neither FFS nor any existing transition path sampling method has been used to study wetting transitions.

Between the two low energy basins the phase space is divided into interfaces in the order parameter. The system is started in one low energy basin, and after some equilibration time, a long MD run is performed. Every time the system crosses from basin A across the first interface, λ_0, the configuration is stored. The flux, $\Phi_{A,0}$, is computed from the number of crossings as

$$\Phi_{A,0} = \frac{\text{number of configurations that crossed } \lambda_0}{\text{simulation time}} \tag{1.3}$$

The next step is to randomly choose a configuration from λ_0 and shoot trajectories to the next interface. States are either stored when they hit the next λ_i interface, or stopped when they return to basin A. This is repeated at each interface until basin A or B is reached. The probability of trajectories reaching basin B is used to compute the transition rate:

$$k_{A\to B} = \Phi_{A,0} P(\lambda_{n=B}|\lambda_0) \tag{1.4}$$

where $P(\lambda_{n=B}|\lambda_0)$ is the probability of reaching basin B having started at λ_0, and is equal to the product of the probabilities of crossing each stage:

$$P(\lambda_{n=B}|\lambda_0) = \prod_{i=0}^{n-1} P(\lambda_{i+1}|\lambda_i) \tag{1.5}$$

There are various techniques for selecting configurations and shooting trajectories to get to basin B, including Direct, Branched Growth [1], and Constrained Branched Growth (CBG) [31]. The later was used for this report as it is the most efficient method, does not require unbiasing and does not result in an explosion of number of runs.

In CBG[31] (illustrated in 1.5), one configuration is selected randomly from the set of configurations stored at λ_0. M_0 trajectories are launched from this starting configuration. The number of trajectories that successfully reach each next interface, λ_i, is given by $N_s^{(i-1)}$. From this set, L_i states are randomly selected. A constant total number of trajectories, M_i, are fired, where M_i is fixed for $0 < i < N$. k_i^j trajectories are launched from each of the L_i states. Parameter values are shown in the Appendix. The value of L_i is selected such that

$$L_i \;=\; \begin{cases} \frac{M_i}{k_{min}}, & \text{for } N_S^{(i-1)} > \frac{M_i}{k_{min}} \\ N_s^{(i-1)}, & \text{for } N_S^{(i-1)} \leq \frac{M_i}{k_{min}} \end{cases} \tag{1.6}$$

where k_{min} is the minimum number of shots per point, and

$$k_i^j \approx \frac{M_i}{L_i} \tag{1.7}$$

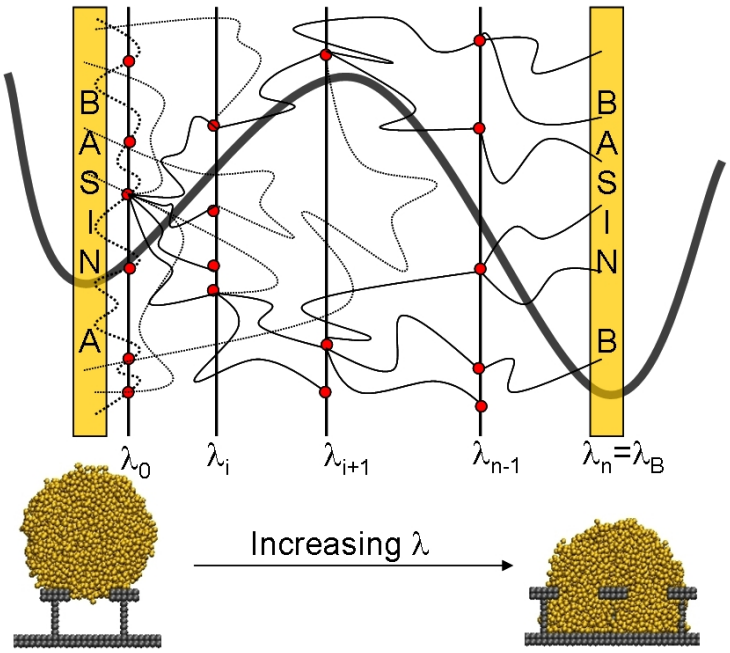

Figure 1.5: Constrained Branched Growth Forward Flux Sampling. Solid vertical black lines are order parameter interfaces. Thin curved lines are trajectories launched from each interface toward basin B, where solid lines successfully reach the next interface and dotten lines returned to basin A. Red dots are configurations stored from successful trajectories. The large black W-shaped curve is an illustrative free-energy landscape.

The overall probability is then

$$P(\lambda_{n=B}|\lambda_0) = \prod_{i=0}^{n-1} \frac{N_S^{(i)}}{M_i} \tag{1.8}$$

The transition rate for each system studied here was estimated as the average $k_{A\to B}$ from approximately 13 runs. A run starts with one randomly chosen starting configuration at λ_0. Following Ref. [30] the decay of the auto-correlation function of the primary order parameter is used to ensure the selected starting configurations are uncorrelated.

The collection of configurations along the reaction coordinate that successfully reach basin B make up the transition path ensemble (TPE). Each point along the TPE has some probability of reaching basin B. This committor probability, p_B, is

computed as

$$p_{B_j}^i = \frac{1}{k_i} \sum_{m=1}^{N_j^i} p_{B_m}^{i+1}, \quad i = n-1, n-2, ..., 0 \tag{1.9}$$

where N_j^i is the number of points reaching λ_{i+1} from point j at λ_i, as described in Refs. [13, 5, 6]. p_B is used to identify the transition state (where p_B=0.5) and the most appropriate reaction coordinate. Visualization of the configurations in the TPE and fitting of order parameters of interest can also give insight to the transition mechanism.

1.4.2 Order parameter

The primary order parameter, λ, is the fraction of particles below the top level of the nail plate. Although this order parameter works well for a droplet that is filling one or two cavities, it does not adequately track the transition when multiple cavities are being filled, for example as the drop size increases. In that case, up and down fluctuations of droplet particles result in multiple intermediate configurations with the same value of the order parameter, many of which do not encourage transition. Although λ was used as the order parameter for all the FFS runs, there may be a more efficient choice, as described in a later section.

1.5 Results

1.5.1 Transition mechanism

Examining snapshots from transition pathways (TPE) of a variety of system sizes, chemistries and nails, one consistent observation is that the transition state is

identified ($p_B = 0.5$) as the point where particles from the droplet first touch the bottom surface. Once this happens the drop easily transitions. The smallest droplet always penetrates the surface by moving between two nails, which should be fairly obvious from 1.3. As the drop gets larger with respect to the roughness features, it can either penetrate two cavities at once (1.6 top), or penetrate one cavity and then spread to fill two cavities (1.6 bottom).

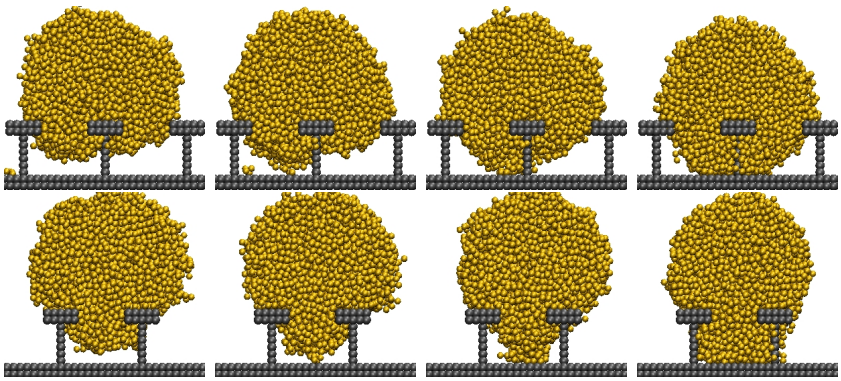

Figure 1.6: Two transition pathways for 4000 particle drop on short nails, $\epsilon = 0.5$. Top: filling two cavities at once; Bottom: filling one cavity before spreading. From left to right: before transition, just before transition state, just after transition state, after transition.

1.5.2 Transition rates

Composite-to-wetted transition rates for the systems shown in 1.3 were computed using FFS. The rates are shown in 1.7, for the slightly phobic (top) and slightly phillic (bottom) chemistries (see 1.1). The rates on the short nails (red triangles) are consistently faster than on the tall nails (black filled circles), as expected. Additionally, the phillic drops transition faster than the corresponding phobic drops. To illustrate the effect of the re-entrant geometry on transition rates, we find that the FFS rate for a 4000 particle phobic drop on short square "posts" (of $5 \times 5\sigma^2$ cross section and $\phi_s = 0.16$) is 7 orders of magnitude faster than that for the same

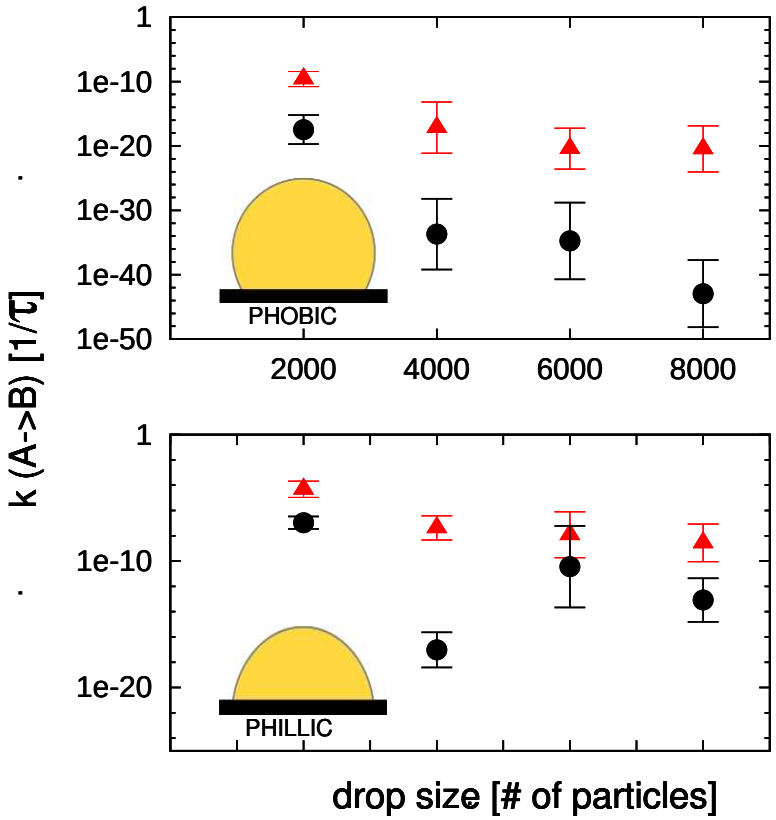

Figure 1.7: Transition rates for droplets of different sizes using phobic (top, $\epsilon_{12} = 0.5$) and phillic (bottom, $\epsilon_{12} = 0.7$) chemistry, on short (red triangles) and tall (black circles) nails. Note that k=1E-16τ^{-1} corresponds to approximately 1 hour transition time using critical properties of dodecane as a reference. Error bars are computed based on log(k).

drop on "nails" of equal height and chemistry.

As the system size gets larger, the rates decrease. This is due to the fact that the diameter of the small drop is nearly the same as the nail spacing, so the drop can readily transition by filling one cavity. But as the drop gets larger, it must fill two cavities at once and/or become unspherical to fill one cavity. In particular, for the 8000 particle drop with the phobic chemistry, the rate for the taller nails is nearly 20 orders of magnitude slower than on the short nails. This is due to the fact that on the taller nails the phobic drop has to distort in order to penetrate the cavities, as it is held back by the outer nails. On the other hand, the phillic drop

remains quite spherical until just before transitioning because the drop particles are able to wrap around the outer nails due to the increased attraction. Snapshots of the phobic and phillic 8000 particle drop just before the transition point (when particles first touch the bottom surface) are shown in 1.8. This is one way in which the relative size of the drop to roughness features plays a role in the wetting behavior.

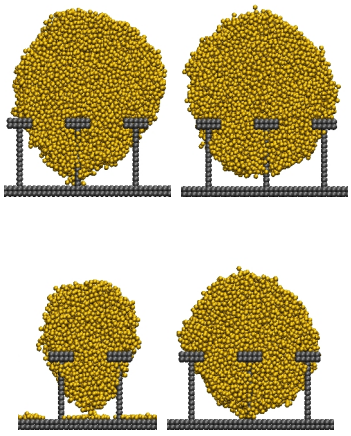

Figure 1.8: Droplet deformation on tall nails just before transition point. Top: 8000 particles, phobic(left), phillic (right); Bottom: phillic, 4000 particles (left), 6000 particles (right).

Notice also in 1.7 that the 4000 particle drop with phillic chemistry on tall nails seems to be an outlier as it has a much lower rate which does not fit the trend. Looking closely at the configurations just before the transition point for the 4000 and 6000 particle phillic drop on tall nails, we see a similar causal phenomenon as noted above. That is, due to the relative size of the 4000 particle drop to the nail spacing, the drop must deform significantly in order to transition, whereas the 6000 particle drop is large enough to spread to a third nail and maintain more of a spherical shape as shown in 1.8. This is pronounced for the phillic chemistry because the top part of the drop wants to stay spread across the nail plates, which exacerbates the deformation.

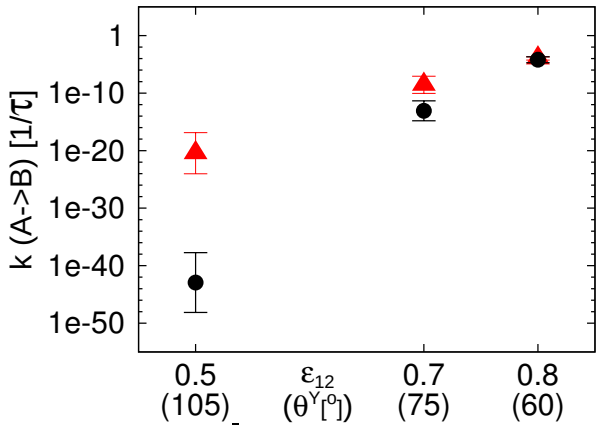

Figure 1.9: Effect of intrinsic chemistry on transition rates of 8000 particle drop on short (red triangles) and tall (black circles) nails.

In addition to the two chemistries discussed above, several runs were also done using a more phillic drop to better understand the effect of chemistry vs. roughness. (See 1.1 for values.) Transition rates are plotted vs. intrinsic chemistry in 1.9, for the 8000 particle drop on both short and tall nails. As the drop becomes more phillic, the chemistry dominates over roughness. This is again due to the fact that the more phillic drop can maintain its spherical shape as it transitions. These results support the importance of surface chemistry in addition to roughness as there is a very large difference in transition rate for a moderate increase in θ^Y from 60^o to 75^o.

Tuteja et. al. [28] introduced a robustness parameter, H^*, to quantify the stability of the composite state. H^* is a dimensionless parameter that is an estimate of the static pressure required to force the drop into the wetted state, scaled by the characteristic capillary rise height. Based on their contact angle measurements of octane on silanized microhoodoos, when H^* is above $\approx$10 the composite state was observed. Choi et. al. [8] tuned H^* by applying strain to a fabric with re-entrant geometry, and show that the composite state is observed for higher values of H^*, with a transition to the wetted state as H^* decreases. This macroscopic

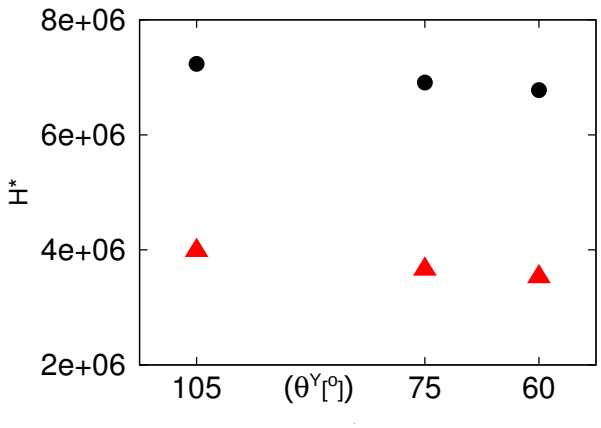

Figure 1.10: Robustness parameter, H^* for short (red triangles) and tall (black circles) nails as a function of intrinsic surface chemistry.

robustness parameter can be compared qualitatively to our kinetic estimates of the transition energy barrier as represented by the transition rates. 1.10 shows H^* values for our system, using the formula for microhoodoos, $H^* = 2[(1 - cos\theta^Y)R + H]l_{cap}/D^2$ where $l_{cap} = \sqrt{\gamma_{lv}/\rho g}$. Note that our H^* values are very large due to the disparity between the macroscopic l_{cap} and our length scale, σ. Both H^* and the FFS transition rates indicate that 1) The more phobic chemistry is more likely to maintain the composite state, 2) taller nails are more likely to maintain the composite state, and 3) nail height has a larger impact than chemistry. However, the transition rates show that the chemistry dominates when it becomes very phillic, whereas H^* suggests the tall nails are still significantly more robust even for very phillic chemistry. H^* assumes a simple dependency on geometry and θ^Y, and hence does not account, e.g., for such effects as the interplay between the drop spreading (over nail tops) and deformation (to fill the cavities).

1.5.3 Optimized order parameter

The committor probability, p_B, can be seen as an ideal reaction coordinate that captures the quantitative progress of the process going from basin A to basin B. It can also be used to identify the transition state, as the ensemble of configurations for which $p_B = 0.5$; i.e., when the system is equally likely to return to basin A or continue to basin B. Although one order parameter is used to run the FFS simulations, we can use the stored configuration files from the TPE to compute other order parameters and look at their correlation with p_B, using a combination of linear and quadratic terms, to find the best fit to describe transition progress. In this case we consider the order parameters listed and described in 1.2. Several other order parameters were tried, including the height of the lowest particle in the cavity and the potential energy between the droplet and surface particles, but the set presented in 1.2 has the most uncorrelated and potentially descriptive parameters.

ID	**Order Parameter**
λ	fraction of particles below top of nail plate
Λ	density of particles in the most filled moving cavity, where the cavity width is fixed but the starting and ending location change in steps of 1 σ such that every possible cavity location (in x) is checked and then the maximum is used (see 1.11)
θ	contact angle

Table 1.2: Candidate order parameters

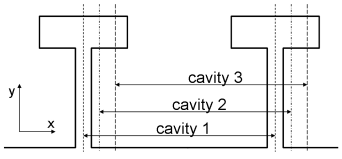

Figure 1.11: Fixed cavity width, but moving location in steps of 1 σ.

Committor probability data was least-squares-fit to linear combinations of the following order parameters:

1. λ
2. λ, λ^2
3. $\lambda, \lambda\Lambda$
4. Λ, Λ^2
5. $\Lambda, \Lambda^2, \theta, \theta^2$

The resulting R^2 values are shown in 1.12. The primary order parameter, fraction of particles below the surface (λ), has a wide range of R^2 values, indicating that for many of the systems λ is not a good order parameter, in particular most of the phobic ($\epsilon_{12} = 0.5$) systems where $R^2 < 0.4$ for all but the smallest droplets. Although this does not necessarily affect the accuracy of the rate calculation, it does result in less than ideal efficiency.

Adding the quadratic term ($p_B = c_0 + c_1\lambda + c_2\lambda^2$) improves the fit slightly for a few systems. The best overall fit is $p_B = c_0 + c_1\lambda + c_2\Lambda + c_3\lambda\Lambda$; ($c_0 - c_3$ are fitting coefficients), which includes the primary order parameter and also the cross term with the density in the most filled moving cavity. In fact this fit gives $R^2 > 0.5$ for all systems except one: the 6,000 particle phobic drop on tall nails. This is the droplet that must deform the most in order to transition. For the 4000 particle drops on short nails, the fits for the phobic and phillic chemistry are, respectively,

$$p_B = 1.0 - 19.7\lambda - 1.8\Lambda + 42.3\lambda\Lambda \quad (1.10)$$

$$p_B = 1.1 - 15.8\lambda - 3.0\Lambda + 46.4\lambda\Lambda \quad (1.11)$$

Other systems have fits with coefficients having similar order of magnitude.

In general, the order parameters which capture both the droplet distorting and reaching toward the bottom surface in a narrow region are the best types of order

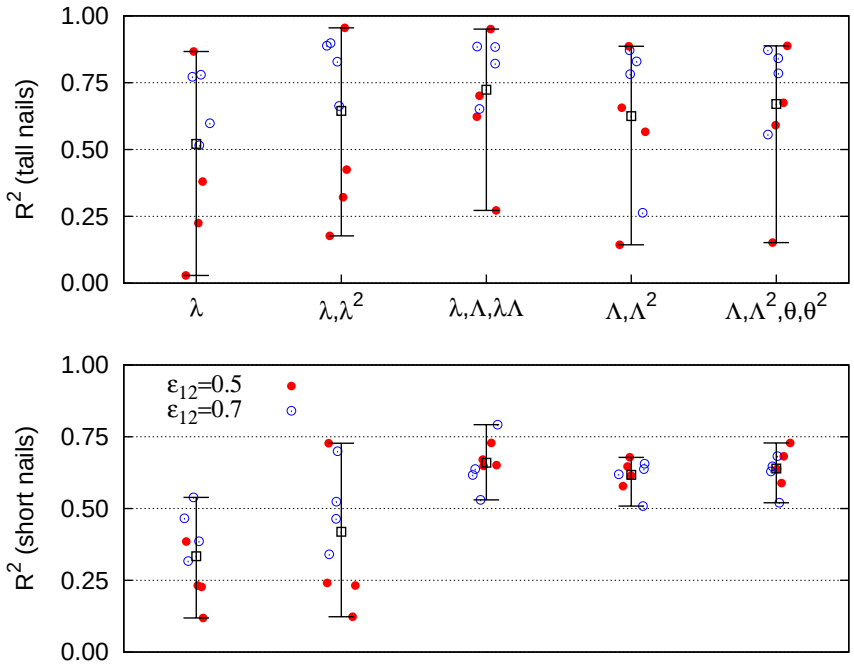

Figure 1.12: R^2 from least squares fit of several combinations of order parameters with p_B. λ, Λ and θ are described in 1.2. Each point represents one system size, one nail height, and one ϵ_{12}. Error bars and black squares show the range and mean value of each set. Top: Tall nails; Bottom: Short nails.

parameters. This reflects the idea that the transition interface is not flat, but the fluctuations that cause the particles to reach out are what cause the droplet to transition and should be disrupted to prevent wetting.

A modified order parameter of $\lambda + \Lambda^2$ was used in a second set of runs for the 4000 particle phobic drop on short nails. This order parameter results in similar transition rates, with smaller error bars by a factor of 2 (based on 20 runs). It also improved the p_B model fit to $R^2 = 0.9$, with slightly different coefficients:

$$p_B = 0.5 - 10.2\lambda - 1.5\Lambda + 30.1\lambda\Lambda \tag{1.12}$$

Efficiency was greatly improved as well. For this system size, comparing the original (λ) to modified ($\lambda + \Lambda^2$) order parameter, the average run time per successful pathway was 66 vs. 4 fs, and the average compute time per full FFS run was 700

vs. 80 CPU hours.

1.6 Conclusions

Molecular dynamics simulations were used to study the wetting behavior of an oily fluid on a rough surface. The re-entrant structure of the model nail surface does create a barrier to fluid transition from the composite to wetted state. Based on kinetic information from FFS rate calculations, such a structure is very effective at preventing transition given a phobic chemistry, but as the fluid becomes more phillic the barrier becomes less effective. Increasing the height of those nails makes the composite state more stable, although for the most phillic chemistry tested here ($\theta^Y = 60^o$), chemistry dominates and the transition happens quickly for both short and tall nails for any drop size. Given that surface energies with intrinsic chemistries up to $\theta^Y = 75 - 80^o$ are possible, it is worth noting that these results (1.9) suggest that a small increase in θ^Y makes roughness feature height a viable "knob" in preventing transition.

Based on kinetic limitations, the slightly phobic drops (except those smaller than the roughness feature spacing) would take $\approx$ thousands of hours to transition, indicating their stability in the composite state. On the other hand, although the nails do provide a barrier which generally increases with drop size and nail height, most of the slightly phillic drops will still transition quickly (one hour or less). Practically speaking, if the transition time can be increased to the order of hours, this would be useful for applications where the droplets can be removed before transitioning. This could likely be achieved by taller nails, or possibly by changing the nail spacing or shape; the latter two variations are subjects of future work.

Transition state configurations consistently show that drops of any size will overcome the free energy barrier and wet once fluid particles first touch the bottom surface. The transition interface at that point is not flat but has undergone significant fluctuation in curvature. Disrupting these events and preventing the particles from reaching the bottom surface should be a design goal to prevent wetting, for example, by making the cavities very deep or creating multiple levels of re-entrant geometry.

Using FFS and MD, we are able to get detailed information about transition kinetics and mechanism, but are limited to small droplets and a few fixed variations of roughness size and chemistry. We are currently using the same techniques to study a bulk fluid, as a limiting case for a very large droplet. Our initial results using BXD [14] to compute the free energy landscape indicate qualitative agreement with the conclusions presented here. Those results also indicate a hysteresis in the wetting vs. non-wetting behavior, consistent with several FFS runs to compute a reverse transition rate, all of which support the picture of an essentially irreversible wetting transition.

While connecting our kinetic results to macroscoic behavior is non-trivial, we expect that qualitative trends should remain consistent and that semiquantitative comparisons could be attempted once results from bulk-like drop simulations and free energy calculations are completed. Note that free energy barriers computed with macroscopic models such as a Gibbs free energy model and the robustness parameter, H*, give much higher values than those observed experimentally [28]. For octane on silanized microhoodoos ($\phi_s = 0.11, \theta^Y = 60^o$), Tuteja et. al. computed a free energy barrier $\Delta G^* = 8.17 \times 10^{-5}$ J/m^2. Our initial BXD estimates of ΔG^* on a less phillic surface ($\theta^Y = 75^o$) with closer nails ($\phi_s = 0.16$) are of

the same order of magnitude, although the difference in chemistry and roughness should produce a larger energy barrier. In other words, BXD applied to the same surface is expected to result in a lower free energy barrier, more in line with experimental results. On the other hand, the raining method predicts unphysically too small values for ΔG^* (O(1) kT) for phobic nails with the same spacing ($\phi_s = 0.25$) and chemistry ($\theta^Y = 100^o$) as the posts used in [18]. These results illustrate the need for more rigorous methods, such as BXD, to account for surface fluctuations in finding the free energy landscape. This work is underway and will be the topic of a future report.

1.7 Appendix

1.7.1 Quantifying LJ units

We evaluate the energy scale, ϵ, by comparing the critical temperature of tridecane ($T_c = 676$K)[15] to that for a fully flexible LJ fluid of tetramers ($T_c^* = 2.2$)[4], which gives $\epsilon = 4.24 \times 10^{-21}$ J.

The length scale, σ, is found from properties of tridecane ($M = 184.361$ g/mol, $\rho = 0.7564$ g/cm^3 $= 4.1 \times 10^{-3}$ mol/cm^3)[15], a typical alkane. Comparing again to the density of the LJ fluid of tetramers ($\rho = 0.8554$ monomers/$\sigma^3 = 3.55 \times 10^{-25}$ mol/σ^3 at $T = 1.0$)[4] gives $\sigma = 0.44$ nm.

Next the temperature-dependent surface tension (γ) of tridecane was compared to that from the LJ tetramer fluid [4] at various values of r_c. The best match is for $r_c = 3\sigma$, where $\gamma \approx 19$ mN/m at 370K for both tridecane and the LJ fluid, and

the temperature dependence is similar.

We can also evaluate the time unit, τ, as follows (Note that m is the mass of 1 bead):

$$\tau = \sigma\sqrt{m/\epsilon} = 4.2 \times 10^{-10} \text{ m} \left(\frac{7.6 \times 10^{-26} \text{ kg}}{4.24 \times 10^{-21} \text{ J}} \right) = 1.8 \text{ ps} \tag{1.13}$$

The default timestep of 0.005τ is then ≈ 9 fs.

1.7.2 CBG parameters

The following CBG parameters were used in the FFS runs:

$$\begin{aligned} M_0 &= 250 \\ M_i &= 50 \text{ for } (0 \text{ ¡ i ¡ N}) \\ k_{min} &= 5 \end{aligned}$$

1.7.3 Selection of λ_0

As described in Ref. [31], selection of the first stage, λ_0, is crucial for a representative transition path ensemble (TPE) and accurate transition rate. The value should be chosen such that the system has started to climb out of basin A. Additionally, since the starting point for each FFS run will be randomly selected from the configurations at λ_0, a sufficient number should be stored such that the full energy landscape is more likely to be sampled. One way to ensure good sampling at and selection of λ_0 is to compare the λ_0 sampling to the phase space coverage of a long run in basin A, plotting the primary order parameter against a secondary orthogonal order parameter. In 1.13, for the 8000 particle droplet on short nails

with $\epsilon_{12} = 0.5$, we plot the primary order parameter (shown as λ/λ_B to indicate extent of reaction) against the contact angle, θ. The two key observations are that 1) the selected value of λ_0 is sufficiently to the right half of the basin A phase space coverage so the systems will have started the climb out of basin A, and 2) there are enough configurations stored at λ_0 to represent the full landscape.

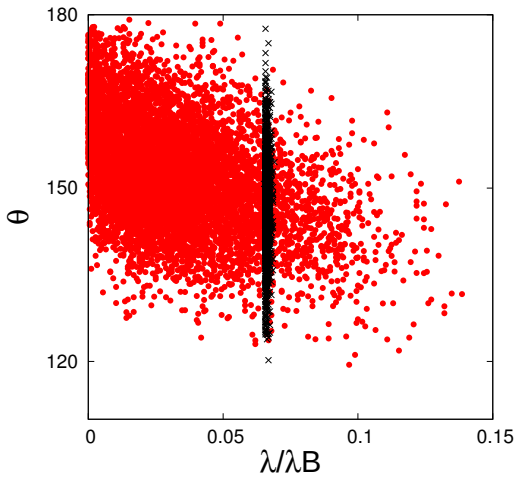

Figure 1.13: Red dot: Basin A phase space coverage; Black x: λ_0 crossings

For the first interface, $\lambda_{0,phobic} = \{0.06, 0.03, 0.02, 0.015\}$, $\lambda_{0,phillic} = \{0.1, 0.05, 0.035, 0.03\}$ for the four system sizes {2K, 4K, 6K, 8K}, respectively.

1.7.4 Dynamic λ spacing

In order to expedite and better automate the FFS runs all the way from basin A to B, a slight modification was made to the CBG method. As before, an initial complete run is done to establish appropriate λ spacing. This spacing is used as the starting point for all remaining runs. However, when a stage $i+1$ is reached where less than two (out of fifty) trajectories from stage i reach $i+1$, the configurations at stage $i+1$ are deleted and an additional stage is inserted halfway between i and $i+1$. Note that in our calculation of the rate, each starting configuration has

equal statistical weight, which, strictly speaking, should not be the case if the λ staging is different from one run to the next. The differences are expected to be small for this system, and the λ staging does not vary much, so the equal-weight assumption is at least a good approximation. Typical λ spacing is shown in 1.14.

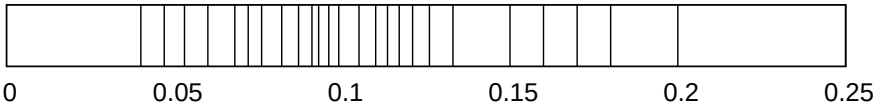

Figure 1.14: Typical λ spacing, shown for the 4000 particle phobic drop on short nails

1.7.5 Nomenclature

Symbol	Meaning
$c_0 - c_3$	fitting coefficients for optimizing order parameter
m	mass of a particle
ΔG	thermodynamic free energy difference between basins A and B
ΔG^*	kinetic transition free energy barrier
H^*	robustness parameter for stability of composite state [28]
$k_{A\to B}$	transition rate from basin A to basin B
k_B	Boltzmann constant
K	energy constant in FENE potential
k_i^j	number of trajectories launched from each of the L_i states selected in CBG method
L_i	number of states randomly selected from successful trajectories at each interface in CBG method
M_i	number of trajectories launched from given starting configuration at interface i in CBG method
N	number of fluid particles
$N_s^{(i-1)}$	number of trajectories that successfully reach each next interface in CBG method
$P(\lambda_{n=B}\|\lambda_0)$	the probability of reaching basin B having started at λ_0
p_B	committor probability for trajectories to reach basin B
r	separation between particles
r^*	reduced separation between particles

Continued on next page

Nomenclature – continued from previous page

Symbol	**Meaning**
r_c	cutoff distance
R_0	maximum extent of FENE bond
T	system temperature
T^*	reduced system temperature
U	potential energy
V	volume of fluid
$\Delta\theta$	contact angle hysteresis
ϵ	LJ potential well depth, and system energy scale
ϵ_{12}	LJ potential well depth between fluid and surface
ϕ_s	fraction of solid in contact with liquid
$\Phi_{A,0}$	flux of trajectories reaching λ_0 from basin A
γ_{SV}	surface energy between solid and vapor
γ_{SL}	surface energy between solid and liquid
γ_{LV}	surface energy between liquid and vapor, i.e. surface tension
γ	surface tension
γ^*	reduced surface tension
λ	order parameter, fraction of particle below top of nail plate
λ_i	order parameter value at interface i
Λ	density of particles in the most filled moving cavity
ρ	fluid density
ρ^*	reduced fluid density
σ	minimum separation distance between particles and system length scale

Continued on next page

Nomenclature – continued from previous page

Symbol	Meaning
θ	contact angle
θ^{CB}	Cassie-Baxter (equilibrium composite) contact angle
θ^{W}	Wenzel (equilibrium wetted) contact angle
θ^{Y}	Young's (intrinsic) contact angle
θ_c^{Y}	Critical intrinsic contact angle
τ	system time scale

Bibliography

[1] Rosalind J Allen, Daan Frenkel, and Pieter Rein ten Wolde. Forward flux sampling-type schemes. *J. Chem. Phys.*, 124:194111, 2006.

[2] Rosalind J Allen, Patrick B Warren, and Pieter Rein ten Wolde. Sampling rare switching events in biochemical networks. *Phys. Rev. Lett.*, 94:018104, 2005.

[3] Rosaline J Allen, Daan Frenkel, and Pieter Rein ten Wolde. Simulating rare events in equilibrium or nonequilibrium stochastic systems. *J. Chem. Phys.*, 124:024102, 2006.

[4] Felipe J Blas, Luid G MacDowell, Enrique de Miguel, and George Jackson. Vapor-liquid interfacial properties of fully flexible lennard-jones chains. *J. Chem. Phys.*, 129:144703, 2008.

[5] Peter G Bolhuis, David Chandler, Christoph Dellago, and Phillip L Geissler. Transition path sampling: Throwing ropes over rough mountain passes, in the dark. *Ann. Rev. Phys. Chem.*, 53:291–318, 2002.

[6] Ernesto E Borrero and Fernando A Escobedo. Folding kinetics of a lattice protein via a forward flux sampling approach. *J. Chem. Phys.*, 125:164904, 2006.

[7] A B D Cassie and S Baxter. Wettability of porous surfaces. *Trans. Faraday Soc.*, 40:546–551, 1944.

[8] Wonjae Choi, Anish Tuteja, Shreerang Chhatre, Joseph M. Mabry, Robert E. Cohen, and Gareth H. McKinley. Fabrics with tunable oleophobicity. *Adv. Mater.*, 21:2190–2195, 2009.

[9] Fernando A Escobedo, Ernesto E Borrero, and Juan C Araque. Transition path sampling and forward flux sampling. applications to biological systems. *J. Phys.: Condens. Matter*, 21:333101, 2009.

[10] C W Extrand. Modeling of ultralyophobicity: Suspension of liquid drops by a single asperity. *Langmuir*, 21:10370–10374, 2005.

[11] Daan Frenkel and Berend Smit. *Understanding Molecular Simulation*. Academic Press, 2nd edition, 2002.

[12] Hiroaki Fukunishi, Osamu Watanabe, and Shoji Takada. On the hamiltonian replica exchange method for efficient sampling of biomolecular systems: Application to protein structure prediction. *J. Chem. Phys.*, 116:9058–9067, 2002.

[13] Phillip L Geissler, Christoph Dellago, and David Chandler. Kinetic pathways of ion pair dissociation in water. *J. Phys. Chem. B*, 103:3706–3710, 1999.

[14] David R Glowacki, Emanuele Paci, and Dmitrii V Shalashilin. Boxed molecular dynamics: A simple and general technique for accelerating rare event kinetics and mapping free energy in large molecular systems. *J. Phys. Chem. B*, 113:16603–16611, 2009.

[15] William M Haynes, editor. *CRC Handbook of Chemistry and Physics*. CRC, 91st edition, 2010.

[16] Chien-Te Hsieh, Fang-Lin Wu, and Wei-Yu Chen. Superhydrophobicity and superoleophobicity from hierarchical silica sphere stacking layers. *Mater. Chem. Phys.*, 121:14–21, 2010.

[17] R E Johnson and R H Dettre. Contact angle, wettability and adhesion. *Adv. Chem. Ser.*, 43:112–135, 1964.

[18] Takahiro Koishi, Kenji Yasuoka, Shigenori Fujikawa, Toshikazu Ebisuzaki,

and Xiao Cheng Zeng. Coexistence and transition between cassie and wenzel state on pillared hydrophobic surface. *PNAS*, 106:8435–8440, 2009.

[19] Kurt Kremer and Gary Grest. Dynamics of entangled linear polymer melts: A molecular-dynamics simulation. *J. Chem. Phys.*, 92:5057–5086, 1990.

[20] Ramasamy Thangavelu Rajendra Kumar, Klaus Bo Mogensen, and Peter Bøggild. Simple approach to superamphiphobic overhanging silicon nanostructures. *J. Phys. Chem. C*, 114:2936–2940, 2010.

[21] Satish A Mahadik, Mahendra S Javale, S K Mukherjee, and A Venhateswara Rao. Transarent superhydrophobic silica coatings on glass by sol-get method. *Appl. Surf. Sci.*, 257:333–339, 2010.

[22] Abraham Marmur. Wetting on hydrophobic rough surfaces: To be heterogeneous or not to be? *Langmuir*, 19:8343–8348, 2003.

[23] M Nosonovsky. Multiscale roughness and stability of superhydrophobic biomimetic interfaces. *Langmuir*, 23:3157–3161, 2007.

[24] Joonsik Park, Hyuneui Lim, Wandoo Kim, and Jong Soo Ko. Design and fabrication of a superhydrophobic glass surface with micro-network of nanopillars. *J. Colloid Interface Sci.*, 360:272–279, 2011.

[25] Neelesh A Patankar. Transition between superhydrophobic states on rough surfaces. *Langmuir*, 20(17):7097–7102, 2004.

[26] S. Plimpton. Fast Parallel Algorithms for Short-Range Molecular Dynamics (http://lammps.sandia.gov). *J. Comp. Phys.*, 117:1–19, 1995.

[27] Siddarth Srinivasan, Shreerang S Chhatre, Joesph M Mabry, Robert E Cohen, and Gareth H McKinley. Solution spraying of poly(methyl methacrylate) blends to fabricate microtextured, superoleophobic surfaces. *Polymer*, 52:3209–3218, 2011.

[28] Anish Tuteja, Wonjae Choi, Minglin Ma, Joesph M Mabry, Sarah A Mazzella, Gregory C Rutledge, Gareth H McKinley, and Robert E Cohen. Designing superoleophobic surfaces. *Science*, 318:1618–1622, 2007.

[29] Anish Tuteja, Wonjae Choi, Gareth H McKinley, Robert E Cohen, and Michael F Rubner. Design parameters for superhydrophobicity and superoleophobicity. *MRS Bulletin*, 33:752–758, 2008.

[30] Camilo Velez-Vega, Ernesto E Borrero, and Fernando A Escobedo. Kinetics and reaction coordinate for the isomerization of alanine dipeptide by a forward flux sampling protocol. *J. Chem. Phys.*, 130:225101, 2009.

[31] Camilo Velez-Vega, Ernesto E Borrero, and Fernando A Escobedo. Kinetics and mechanism of the unfolding native-to-loop transition of trp-cage in explicit solvent via optimized forward flux sampling simulations. *J. Chem. Phys.*, 133:105103, 2010.

[32] Hongxia Wang, Yuhua Xue, and Tong Lin. One-step vapour-phase formation of patternable, electrically conductive, superamphiphobic coatings on fibrous materials. *Soft Matter*, 7:8158, 2011.

[33] R N Wenzel. Resistance of solid surfaces to wetting by water. *Ind. Eng. Chem.*, 28:988–994, 1936.

[34] Thomas Young. An essay on the cohesion of fluids. *Philosophical Trans. Royal Soc. London*, 95:65–87, 1805.

CHAPTER 2

SIMULATION STUDY OF FREE-ENERGY BARRIERS IN THE WETTING TRANSITION OF AN OILY FLUID ON A ROUGH SURFACE WITH RE-ENTRANT GEOMETRY*

2.1 Abstract

When in contact with a rough solid surface, fluids with low surface tension, such as oils and alkanes, have their lowest free energy in the fully wetted state. For applications where non-wetting by these phillic fluids is desired, some barrier must be introduced to maintain the non-wetted composite state. One way to create this free energy barrier is to fabricate roughness with re-entrant geometry, but the question remains as to whether the free energy barrier is sufficiently high to prevent wetting. Our goal is to quantify the free energy landscape for the wetting transition of an oily fluid on a surface of nails, and identify significant surface features and conditions that maximize the wetting free energy barrier (ΔG^*_{fwd}). This is a departure from most work on wetting, which focuses on the equilibrium composite and wetted states. We use Boxed Molecular Dynamics (BXD) [Glowacki et al., *J. Phys. Chem. B*, **2009**, 113, 16603-16611], with a modified control scheme, to rigorously evaluate both the thermodynamics and kinetics of the transition over a range of chemistries. We find that the re-entrant geometry of the nails does create a free energy barrier to transition for a phillic chemistry whereas a corresponding system on straight posts wets spontaneously, and that doubling the nail height

* Reprinted with permission from Escobedo, F. A.; *Langmuir* **2012**, *28*, 16080-16090. Copyright 2012 American Chemical Society.

more than doubles ΔG^*_{fwd}. For neutral to phillic chemistries the dewetting free energy barrier is at least an order of magnitude higher than that for wetting, indicating essentially an irreversible wetting transition. Transition rates from BXD simulations, and the associated trends, agree well with those of our previous study which used Forward Flux Sampling to compute transition rates on similar systems.

2.2 Introduction

There is extensive research in the literature concerned with designing a surface to have specific wetting characteristics, whether it be to encourage wetting or to repel fluids [14, 7, 43]. Design parameters are related to surface chemistry and topology, as indicated by Young's equation [42], which describes the intrinsic wettability of a surface based on interfacial energies, and the Wenzel [40] and Cassie-Baxter [5] equations, which account for the effect of surface roughness. Analysis of these equations clearly indicate that low surface tension fluids (with intrinsic contact angle, $\theta^Y < 90^o$) will prefer to be in the fully wetted state, and that this preference will be further enhanced by adding surface roughness. [18]. Therefore, preventing wetting by fluids such as alkanes and oils, presents a significant challenge.

One approach that has met some success is to create an energy barrier to prevent the fluid from transitioning from the non-wetted composite state to the wetted state [9, 28] by adding surface roughness with re-entrant geometry, such as nanonails [1], microhoodoos or carefully designed electrospun fibers [34]. A fluid sitting on this surface in the composite state needs to create additional surface area to penetrate beyond the "caps" of the re-entrant geometry, thereby providing a transition energy barrier. While there has been significant experimen-

tal, theoretical and simulation work done to study the equilibrium wetted states [5, 40, 7, 18, 42, 43, 16, 15, 22, 41], less is known about the wetting transition dynamics. The Wenzel and Cassie-Baxter equations predict the static contact angle and which state will be more stable, but it would also be valuable to quantify the stability of a metastable composite state based on surface roughness characteristics.

Some quantification of the wetting transition energy barrier has been done using continuum models based on Gibbs free energy analysis [26, 30], but the assumption of a flat fluid-vapor interface limits the accuracy of such calculations [35]. This could be overcome by treating the liquid-vapor interface as a variable and minimizing the free energy [29], but such an approach may have limited applicability to drops and surface features at small [$< O(10^2)nm$] length scales. Koishi et al. [20] presented a molecular dynamics "raining" method, where the probability of a nanodroplet transitioning to the wetted state at different impact velocities was used to find the wetting transition free energy barrier, ΔG^*_{fwd}. For their system of water droplets on phobic pillars, they computed ΔG^*_{fwd} on the order of 0.1 to 1 kT. This approach gives limited information, and for our systems appears to significantly under predict the free energy barrier, as it favors the wetted state even for phobic chemistries. In the Appendix we describe a modified raining method based on a quasi-equilibrium perspective which, while predicting free energy barriers of the right order of magnitude, results in values that seem too sensitive to undersampling to be useful for our system. Giacomello et al. [11] used restrained molecular dynamics - parallel tempering to evaluate the phase diagrams and free energy barrier of the wetting transition on straight phobic posts of fixed height. They note that rare-event sampling techniques are needed to simulate the transition events due to their observed free energy barriers of > 10 kT, and also observed

a transition interface that is not flat. We recently examined composite to wetted transition rates for oily fluids on a surface of nails [32], and found that the transition is largely kinetically limited, so that the transition rate is a good indication of the apparent stability of the initial composite state.

In the current report we use a modified version of Boxed Molecular Dynamics (BXD) [12] to rigorously quantify the free energy landscape of a fluid droplet on a surface of nails throughout the transition from the composite state to the fully wetted state. We look at the effects of intrinsic surface chemistry and nail height, and compare them to those in corresponding systems on posts which lack any re-entrant geometry. In the Simulation Setup Section we describe details related to simulation and system parameters. In the Methods Section we review how the BXD algorithm is used to find the free energy landscape and transition rates, and describe our modified method of trapping the system within boxes. In the Results Section we present free energies, barriers and transition rates, and finally we draw some conclusions and make comparisons between the different methods.

2.3 Simulation setup

Molecular dynamics simulations were performed using the constant volume and temperature NVT ensemble in LAMMPS [31], with a Langevin thermostat[33] (damping parameter = 20 τ; reduced temperature T^* = 1.0; T = 307 K). The main system consists of a cylindrical droplet made up of 1000 tetramers (4000 fluid particles) of Lennard-Jones (LJ) particles, sitting on a surface of nails. A brief overview is given here, and more detail can be found in our previous report [32]. A secondary system, which we will henceforth refer to as the "bulk" case,

uses 1000 tetramers in a setup that eliminates the contact line and approximates the limiting behavior of a macroscopic fluid. Figure 2.1 shows the bulk system in both low energy basins, the composite and wetted state. A few select conditions are also repeated on a larger system, to be referred to as the "large bulk" case, which has 3000 tetramers (see insets of Figure 2.7).

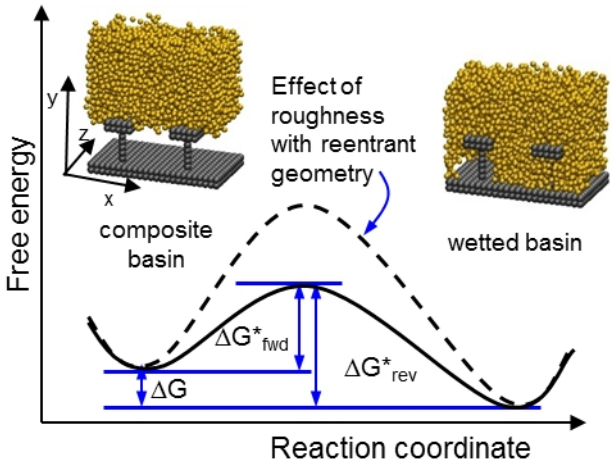

Figure 2.1: Schematics of wetting process going from (left) Cassie-Baxter (composite) non-wetting state to (right) Wenzel, wetting state

The surface is a flat 2 σ thick slab on the bottom, with nails protruding, where σ is the length scale in LJ units. The nail posts underneath are 1σ in diameter, and the plates on top are $5 \times 5\sigma^2$ squares and 2σ thick. They are spaced evenly at a distance of 12 and 13 σ between nail posts in the x and z directions, respectively, giving a constant surface fraction of $\phi_s = 0.16$ for both "drop" and "bulk" systems. The y dimension is normal to the surface. Two nail heights are used: 9σ for the "short" nails and 15σ for the "tall" nails. All surface particles are laid out on a simple cubic lattice with 1σ spacing. Surface particles are fixed by not applying time integration to them.

Several baseline comparisons are made to a system with posts to evaluate the effect of the re-entrant geometry of the nails. The posts have the same $5 \times 5\sigma^2$

cross section (as the nail tops) through the whole height and otherwise have the same spacing, height and properties as the nails.

The overall simulation box size is $60 \times 40 \times 13\sigma^3$ for the droplet and the large bulk system, and $24 \times 50 \times 13\sigma^3$ for the (regular) bulk system. The latter bulk system is narrower in the x dimension so that the same number of tetramers fully covers two nails and still has enough thickness in the y dimension to leave fluid on top of the tall nails when fully wetted, and taller in the y dimension so the bulk fluid is unconstrained in the composite state. Periodic boundary conditions are used in the x and z dimensions, and the y dimension is fixed with a reflecting wall at the top of the box above the drop. The open space below the bulk fluid does not connect to the vapor space above the fluid.

The interactions between particles within the fluid are defined by the LJ cut and shifted potential ($\epsilon = \sigma = 1.0$). Tetramers are formed by bonding the fluid particles together using the FENE [21] potential ($K = 30\epsilon/\sigma^2, R_0 = 1.5\sigma$). All parameters are defined in LJ units (e.g., $r^* = r/\sigma, T^* = Tk_B/\epsilon$; see Ref. [10]). Based on the properties of tridecane (a representative alkane), $\epsilon = 4.24 \times 10^{-21}$ J, $\sigma = 0.42$ nm, $r_c = 3\sigma$, and $\tau = 1.8$ ps (see Appendix for details on unit evaluation).

Interactions between the fluid and surface also use the LJ potential, with $\sigma = 1.0$. The intrinsic wetting behavior, characterized by the contact angle (θ^Y) of the fluid on a flat, homogeneous surface, is determined by the well depth parameter, ϵ_{12}. This relationship was established by a series of simulation on a flat surface, as described in Ref. [32]. The chemistries used are shown in Table 2.1.

ϵ_{12}	0.3	0.4	0.5	0.6	0.7	0.8
$\theta^Y[^o]$	138	120	105	90	75	60

Table 2.1: Intrinsic Chemistries

2.4 Methods

We used Boxed Molecular Dynamics (BXD) to study both the free energy landscape of wetting transition (our primary goal) and, complemented with Accelerated Dynamics (AXD), the associated transition rates. There are a number of other transition path sampling methods which can be used to find kinetic information for a rare event transition. Transition Interface Sampling (TIS) [37] and Forward Flux Sampling (FFS) [2] divide the system into interfaces along a reaction coordinate and provide transition rate calculations based on the probability of getting from one low energy state to another across the transition. Markovian Milestoning (MM) [39] is similar to BXD in the way the system is divided into boxes, but rate information comes from a description of boundary-to-boundary events rather than box-to-box crossings. MM can be applied to non-equilibrium systems [38] and the scheme parallelized to allow each box's trajectory to run simultaneously. Some variants of these methods can also be used to concurrently collect data to map out free energies [27, 36, 4]. We adopted here BXD and AXD as they have already been well validated, are closely related to other established interfacial-based methods, and appear to provide an appealing combination of simplicity and efficiency.

We briefly review how the BXD, and closely related AXD algorithms are used to find the free energy landscape and transition rates, respectively. In the Appendix, we describe in detail the method which we use to constrain our system within a box (a "window" in order parameter), as it differs from the original velocity-reversal scheme presented by Glowacki et al. [12].

2.4.1 Free Energy via Boxed Molecular Dynamics

BXD is a technique which is used to quantify the free energy landscape and estimate the transition rate as the drop moves from one low free energy basin to another. The system is divided into boxes along some order parameter (λ). Starting from one basin, the system is confined to a box for some time, then allowed to move to the next box and confined there, and so on, until the system has traversed the configurational space back and forth between the two basins enough times for convergence of the box-to-box rate coefficients. This is illustrated in Figure 2.2. The frequency with which the system visits different λ values within a box and collides with the box walls are used to compute the free energy and a transition rate. The key implementation detail is how to best confine the system within a box without disrupting the dynamics. We briefly describe the relevant equations here. For details, see Ref. [12].

The system is divided into m intervals from λ_0 to λ_m, as shown in Figure 2.2. As the system evolves, the amount of time(t_m) within a box bounded by λ_m and λ_{m-1}, and the number of times the system hits a box wall ($h_{m,m-1}$) are tracked and used to compute forward and reverse box-to-box rate coefficients, $k_{m,m-1}$ and $k_{m-1,m}$ as

$$k_{m,m-1} = \frac{h_{m,m-1}}{t_m} \tag{2.1}$$

$$k_{m-1,m} = \frac{h_{m-1,m}}{t_m} \tag{2.2}$$

Once all boxes have been visited and the box-to-box rates coefficients are known, equilibrium constants between neighboring boxes n and $n-1$ are com-

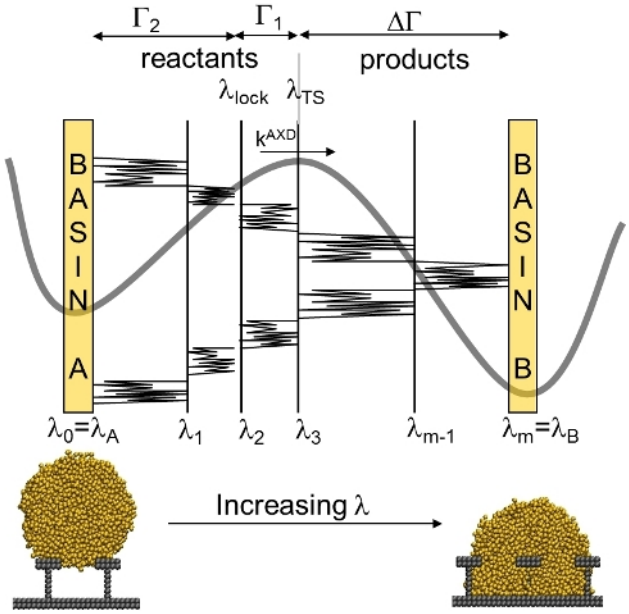

Figure 2.2: Illustration of BXD and AXD techniques. The zig-zag lines represent the trajectory of the system within a box bounded by λ_m and λ_{m-1}. For AXD the space between basins A and B is divided into representative "reactants" and "products", separated by a transition state barrier, λ_{TS}.

puted as

$$K_{n-1,n} = \frac{k_{n-1,n}}{k_{n,n-1}} = \exp\left(-\frac{\Delta G_{n-1,n}}{k_B T}\right) \tag{2.3}$$

By rearranging Eqn. 2.3, the free energy difference between boxes, $\Delta G_{n-1,n}$ can be found. The probability of residing within each box, p_n, is

$$p_n = \frac{1}{\sum_n \exp(-\Delta G_n / k_B T)} \exp(-\Delta G_n / k_B T) \tag{2.4}$$

where ΔG_n is the free energy with respect to some arbitrary zero, and p_n is used to renormalize $p_n(\lambda)$, the probability that the reaction coordinate has some value λ within box n, and find the normalized probability distribution along the

entire reaction coordinate, $p(\lambda)$, as

$$p(\lambda) = p_n(\lambda) \times p_n \tag{2.5}$$

from which the free energy profile is then

$$G(\lambda) = -k_B T \ln p(\lambda) \tag{2.6}$$

One implementation detail that differs from the original method described in Ref. [12] is how the multiple oscillations are traversed. Whereas Glowacki et al. use one long run and travel back and forth multiple times between one low energy basin and another, we select multiple random and uncorrelated starting configurations from basin A and perform one complete oscillation from basin A to B and back to A, for each selected configuration. In this way we are able to run each oscillation in parallel and complete the full set much more rapidly. We performed 10-15 full oscillations for each BXD run, with a minimum of 50 hits on each box wall before moving to the next box (except as otherwise noted).

2.4.2 Estimating the transition rate

Having obtained the box-to-box rate constants and normalized probability distribution, we estimate the overall transition rate using Accelerated Dynamics (AXD) and compare to an analytical solution of the Kinetic Master Equation (KME). If the free-energy landscape has already been mapped out as a function of some order parameter, the rate of rare-event transitions can be estimated by methods that

initialize trajectories near the saddle points [6]. The performance of such methods, however, is known to be highly sensitive to the choice of order parameter.

Accelerated Dynamics (AXD) has a similar implementation to BXD but only divides the configurational space volume into two boxes (see Γ_1 and Γ_2 at top of Figure 2.2). The transition rate is based on the box-to-box rate coefficient across the transition state, k_{AXD}, and a correction factor, P^{CORR}:

$$k_{A\to B} = k_{\mathrm{AXD}} \times P^{\mathrm{CORR}} \tag{2.7}$$

where

$$P^{\mathrm{CORR}} = \frac{\int_{\lambda\in\Gamma_1} p(\lambda)\ \mathrm{d}\lambda}{\int_{\lambda\in\Gamma_1+\Gamma_2} p(\lambda)\ \mathrm{d}\lambda} \tag{2.8}$$

Both k_{AXD}, and P^{CORR} are easily found from the BXD information by positioning the box boundary, λ_{lock}, just before the transition point, λ_{TS}, or the peak of the free energy curve. For more on the derivation of the AXD equations see Ref. [12].

The transition rate can also be computed using a discretized KME to describe the global time dependence and the box-to-box rate coefficients obtained from BXD. [13] We use the analytical solution for the mean first passage time of this KME, described in more detail in Ref. [8], to compute forward and reverse transition rates and compare to the AXD rates. KME assumes a random walk over discrete states, which would ideally be the box walls. But the box-to-box rates from BXD are based on transitions between some average state between two walls. Therefore, there is some arbitrariness in defining precise lambda values for KME which can introduce some boundary artifacts and precludes a precise correspondence between AXD and KME rates. Nonetheless, they are expected to be within

one order of magnitude of each other.

Both methods for computing transition rates can be applied in the forward and reverse directions. The BXD method assumes a Markovian process and so the transition rates are approximate. We compare these transition rates to the Forward Flux Sampling (FFS) rates previously reported [32]. The FFS method is a transition path sampling method where the system is systematically ratcheted from one low energy basin (A) to another (B) along some order parameter. The probability of reaching basin B rather than returning to basin A, and the flux of trajectories leaving basin A, are used to compute the transition rates. FFS provides a more rigorous estimate of the transition rate because it captures true dynamical pathways.

2.5 Results

In this Section we present and discuss the simulated free energy curves, free energy barriers and transition rates obtained from the BXD and AXD methods, and compare the latter to KME rates and previously published FFS transition rates [32].

2.5.1 Free energy

We obtained free energy curves across the transition for several chemistries. Most results are for the short nails, with a few select cases shown for the tall nails. All free energy curves are plotted with respect to fractional progress from basin A to basin B, λ/λ_B. From the free energy curves we extract the forward and reverse

free energy barriers, and the thermodynamic free energy difference between the composite and wetted states. Estimated error bars on free energy curves are about 1 kT at low λ/λ_B and through the wetting transition, and increase to about 3 kT near basin B (λ/λ_B=1). For the large bulk system, error bars are 1-2 kT higher. For systems which exhibit some hysteresis in dewetting, error bars can also increase by 3-5 kT near small intermediate barriers, as discussed below. Error bars are estimated from the differences over all (in most cases, 10) full oscillations for a given set of conditions.

Free energy curves

Figures 2.3 and 2.4 show the free energy curves for the drop wetting transition over a range of chemistries, on nails and posts, respectively. Figure 2.5 shows the same for the bulk system. (Note that for $\theta^Y = 90^o, 120^o, 137^o$, only 10 hits per wall were counted before moving to the next box. While a higher number of hits improves the statistics, we did not see significant differences in the free energy curves in comparing several cases.) The x-axis in both figures shows the order parameter as a fraction of progress from basin A (composite) to basin B, where the drop has wetted the nails and fills two cavities, as shown by the inset configurations in Figures 2.3 and 2.5. Notice that several of the curves for the drop show a slight flattening around $\lambda/\lambda_B = 0.6$. This is the point where the drop has filled one cavity (middle inset configuration of Figure 2.3), and must pause before spreading to the second cavity. These small intermediate wetted state energy barriers were described by Johnson and Dettre [19]. In practice, they are overcome readily by vibrational energy, and the wetted drop will take on the low energy Wenzel state. According to Johnson and Dettre, these intermediate barriers are directly proportional to feature height but do not depend on feature spacing.

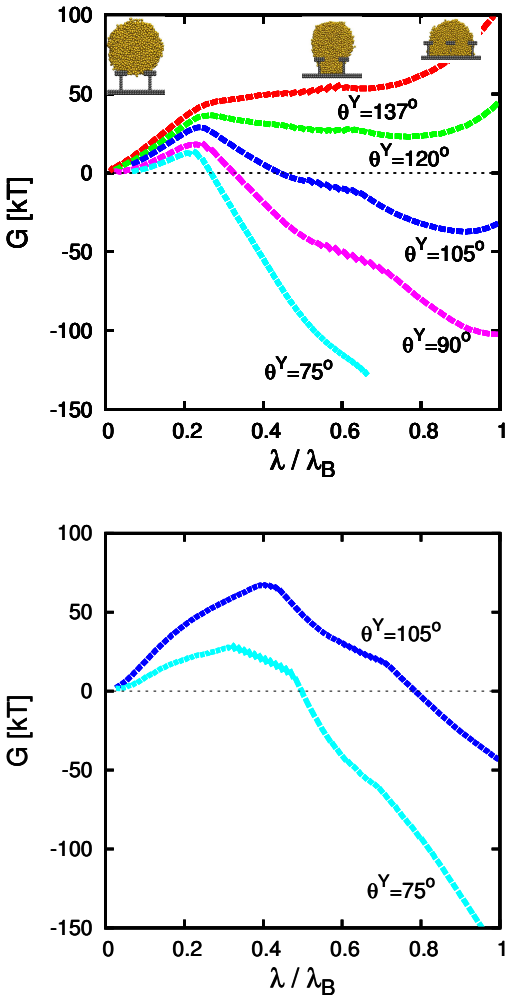

Figure 2.3: Free energy curves for a range of chemistries, for the drop sitting on short (top) and tall (bottom) nails.

The composite to wetted transition point is the first peak in $G(\lambda)$, which occurs around $\lambda/\lambda_B = 0.22$ for the drops on short nails. The most phobic drops ($\theta^Y = 137^o$) will spontaneously dewet as there is no free energy barrier in the reverse direction ($\Delta G^*_{\text{rev}} = 0$), and in the forward direction ΔG^*_{fwd} is very large. The phillic drop ($\theta^Y = 75^o$) does have a barrier to wetting due to the nails, although it is small. The reverse (dewetting) transition has a very large energy barrier indicating that it is essentially irreversible. The behavior is similar on the tall

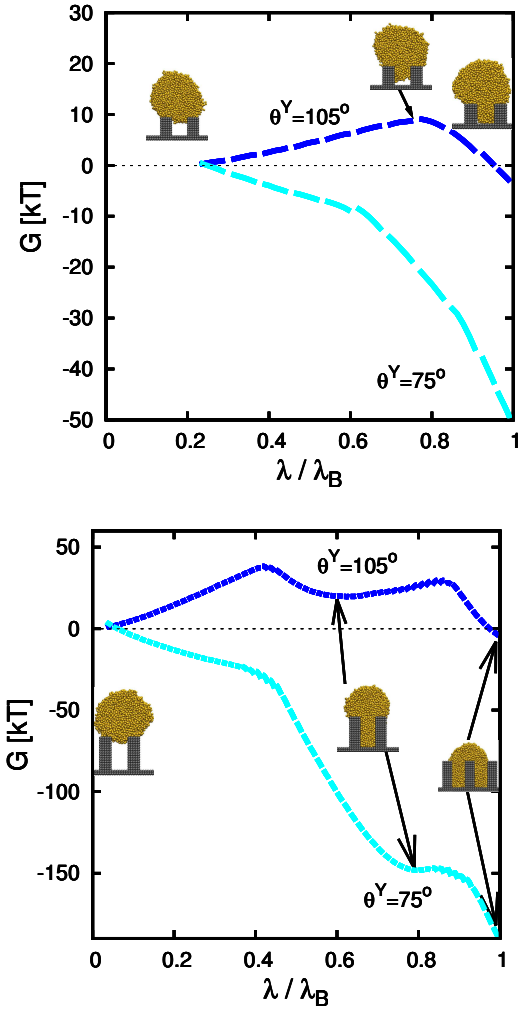

Figure 2.4: Free energy curves for the drop sitting on short (top) and tall (bottom) posts.

nails, with larger energy barrier in the forward and reverse directions. For all drops, visual inspection of configurations reveals that the transition state (corresponding to the leftmost peak of the free energy profile) occurs when particles first touch the bottom surface, consistent with previously published results [32].

To quantify the effect of the re-entrant geometry, the drop and bulk system were also run using posts with the same exposed surface fraction, ϕ_s, and feature height. The resulting free energy curves are shown in Figures 2.4 and 2.5. In all cases,

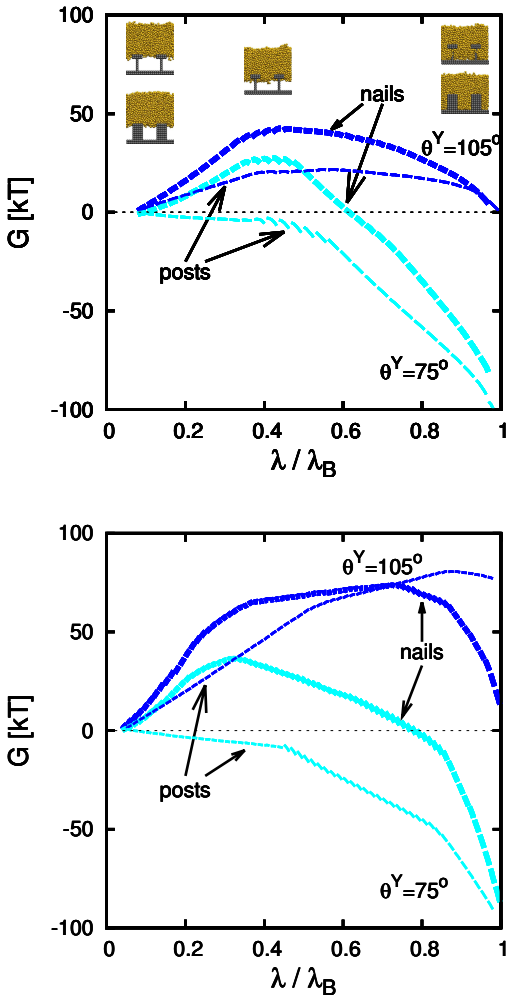

Figure 2.5: Free energy curves for the bulk system sitting on short (top) and tall (bottom) nails and posts, with phobic and phillic chemistries. Basin A and B configurations are shown for short nails and posts, as well as a configuration at the peak of the free energy curve for the system on nails.

the phillic chemistry on posts shows no free energy barrier to wetting, whereas on nails the free energy barrier was between 10-35 kT. For phobic chemistry, the nails increase the wetting free energy barrier by 50 to 250 % as compared to posts. The transition point at the peak of the free energy barrier on phobic posts corresponds to when particles first touch the bottom surface, as shown in the middle inset of Figure 2.4. This is consistent with the drop's behavior on nails.

The true equilibrium free energy curve comes from sampling all regions, and is derived from the combined data from forward and reverse oscillations. Some of the free energy curves are non smooth between $\lambda/\lambda_B \approx 0.5 - 0.7$ (for drops on short nails). To examine the reason for this, we computed $G(\lambda)$ using forward and reverse oscillations separately. As illustrated in Figure 2.6, the wetting and non-wetting curves do not match in such a non-smooth region. A closer look at the configurations show that the drop takes on a different state when wetting or dewetting, as shown in the insets of Figure 2.6. Such a hysteresis signals a lack of pathway reversibility in the region $0.5 < \lambda/\lambda_B < 0.7$. A better order parameter, or a method to more vigorously sample orthogonal degrees of freedom to λ, would allow a more ergodic access to all important pathways and give better estimates of the free energy, especially for ΔG^*_{rev} (note in Figure 2.6 that ΔG^*_{fwd} shows already no hysteresis). The lack of reversibility also violates the Markovian assumption upon which the BXD rate estimate is based, suggesting that, e.g., the dewetting rate will likely exhibit larger errors. The hysteresis could be addressed, for example, by using parallel tempering with the same order parameter described here, similar to the approach adopted by Giacomello et. al. [11]. However, the hysteresis does not jeopardize our conclusions because it is not observed in the wetting pathways used to compute ΔG^*_{fwd}, which is our primary figure of merit. Additionally, the dewetting ΔG^*_{rev} is already sufficiently large as to suggest an essentially irreversible wetting transition, so that moderate errors will not change that conclusion.

For the bulk system (Figure 2.5), we do not see any intermediate, small free energy peak as in Figure 2.3, which is partially a consequence of having only two cavities to fill, and also to the lack of a contact line. With the phobic chemistry, the structure of the system at the top of the free energy barrier is consistent

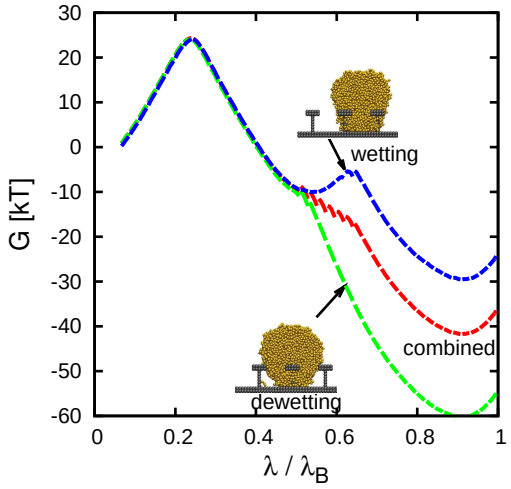

Figure 2.6: Free energy curves for the phobic ($\theta^Y = 105^o$) drop on short nails, computed using forward (wetting, top curve) and reverse (dewetting, bottom curve) oscillations separately, and comparing to the combined oscillations (middle curve). Inset configurations at $\lambda/\lambda_B = 0.62$.

with previous observations of the transition state (i.e., when particles first touch the bottom surface). With phillic chemistry, the behavior of the bulk system is slightly different: the initial region near the top of the energy barrier corresponds to a state where fluid particles wrap around the bottom of the nail plates (see middle inset configuration of Figure 2.5, $\lambda/\lambda_B \approx 0.3$), after which the transition occurs very gradually (as indicated by a relatively flat slope in the phillic free energy curves) up to $\lambda/\lambda_B \approx 0.5$ and 0.8 on the short and tall nails, respectively, which is the point where particles first touch the bottom surface. After this event the transition continues rapidly.

The large bulk system with phobic chemistry (Figure 2.7) has a wetting free energy barrier of 20 kT, which is comparable to the drop with phobic chemistry. Multiple small secondary free energy barriers are seen as the fluid fills the next cavity. There is also evidence of hysteretic behavior at the jump to one more (or one less on dewetting) cavity. The large bulk system has more variety in wetting

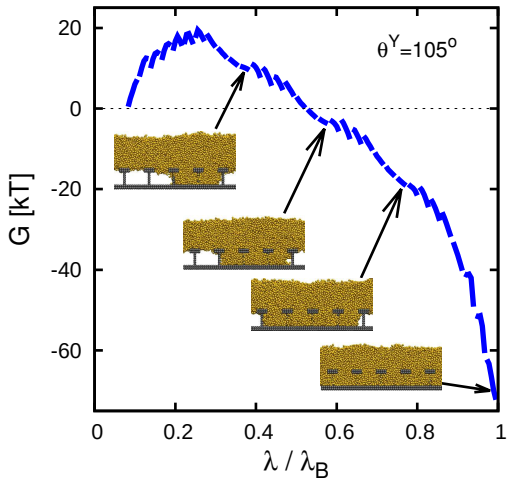

Figure 2.7: Free energy curve for the large bulk system sitting on short nails with phobic chemistry

and dewetting pathways as compared to the regular bulk system, so there is more chance for hysteresis. Indeed, there is even evidence of hysteresis in crossing the first, main free energy barrier from the composite state (i.e., at low λ/λ_B values). In all cases for this large bulk system, the main transition to fill the first cavity occurs quickly once the first fluid particles reach the bottom surface, followed by sequential filling of the remaining cavities. An order parameter which better describes a cavity filling, such as that proposed in our previous report[32], would likely exhibit less hysteresis in the main forward wetting transition. The sequential filling of neighboring cavities is driven by the surface tension of the fluid, and is consistent with the disparity between the small secondary free energy barriers observed and the large barrier (comparable to ΔG^*_{fwd}) that would be required for the fluid in a non-neighbor cavity region to jump to the bottom surface.

Free energy barrier

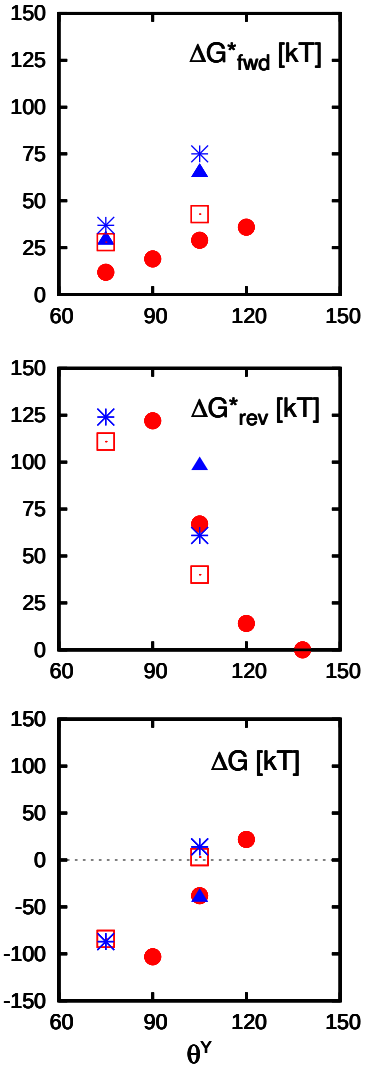

Figure 2.8: Forward and reverse free energy barriers and equilibrium free energy difference computed using BXD. Red filled circles: drop on short nails; Red squares: bulk on short nails; Blue filled triangles: drop on tall nails; Blue stars: bulk on tall nails. Estimated error bars are about 1 kT for ΔG^*_{fwd}, and 3-5 kT for ΔG^*_{rev} and ΔG.

From the free energy curves we can extract the composite to wetted free energy barrier, ΔG^*_{fwd} (see Figure 2.1), which is the primary metric of interest as this is the value we wish to maximize if preventing wetting is the goal. For the cases where the drop makes a full transition to the wetted state, we can also extract

the dewetting energy barrier, ΔG^*_{rev}, as well as the thermodynamic free energy difference between the two states, ΔG. These values are shown in Figure 2.8 for the drop on short (red circles) and tall (blue triangles) nails, and also the bulk fluid on short (red squares) and tall (blue stars) nails.

We can make the following observations:

- A wetting free energy barrier exists for all chemistries and fluid configurations on nails, whereas posts with phillic chemistry the fluid spontaneously wets. This confirms that the re-entrant geometry does, in fact, hinder transition.
- The forward (composite to wetted) transition free energy barrier increases with θ^Y, and approaches 0 at low θ^Y, indicating that for very phillic drops, the chemistry dominates and nail height has little effect. This is consistent with observations based on FFS transition rates reported elsewhere [32].
- The reverse (dewetting) transition free energy barrier approaches 0 for very phobic chemistry, where the drop will spontaneously dewet, and becomes very large at very phillic chemistry, where wetting is essentially irreversible.
- The bulk fluid has higher ΔG^*_{fwd}, and lower ΔG^*_{rev} as compared to the drop. This is consistent with the fact that, per unit area of the top solid surface, the drop has a larger surface area exposed to the gas due to its curvature, and therefore a larger free energy penalty which is alleviated upon transitioning to the wetted state. In contrast, the bulk system has the same surface area exposed to the gas in both composite and wetted state.
- The equilibrium free energy difference increases with θ^Y. Positive values mean the drop prefers to be in the composite state. Note that some phobic drops ($\theta^Y = 105^o$) actually prefer to be in the wetted state, but the corre-

sponding bulk fluid systems prefer the composite state, for reasons described above. The trends with chemistry are the same for the drop and the bulk.

- Doubling the nail height increases ΔG^*_{fwd} by 2-3 times.

2.5.2 Transition rates

Figure 2.9 shows forward and reverse transition rates computed using both the AXD (filled symbols) and KME (open symbols) methods described previously. There is good agreement between the AXD and KME rates, with KME rates being consistently about an order of magnitude lower than AXD rates. Note that error bars in simulated transition rates are typically quite large so that a difference of one to two orders of magnitude can be deemed as acceptable. [13]

Wetting transition rates for the bulk system are 8-12 orders of magnitude lower than for the drop, which is consistent with the corresponding ΔG^*_{fwd} values and reasons described in the Section on free energies (e.g. Figure 2.8).

Overall, the more phillic drops transition to the wetted state much more quickly, and the increase in nail height reduces the wetting transition rate by 10-20 orders of magnitude. For example, the rate with phillic chemistry ($\theta^Y = 75^o$) is reduced to well below the level of phobic chemistry ($\theta^Y = 105^o$) by doubling the nail height. This is consistent with the corresponding ΔG^*_{fwd} values and suggests that increasing feature height could prevent wetting on time scales of interest.

Wetting rates for the drop from previous FFS simulations [32] are also shown in Figure 2.9. Agreement is reasonable for the phillic chemistry, but FFS rates are significantly lower than AXD rates for the phobic chemistry. We expect that

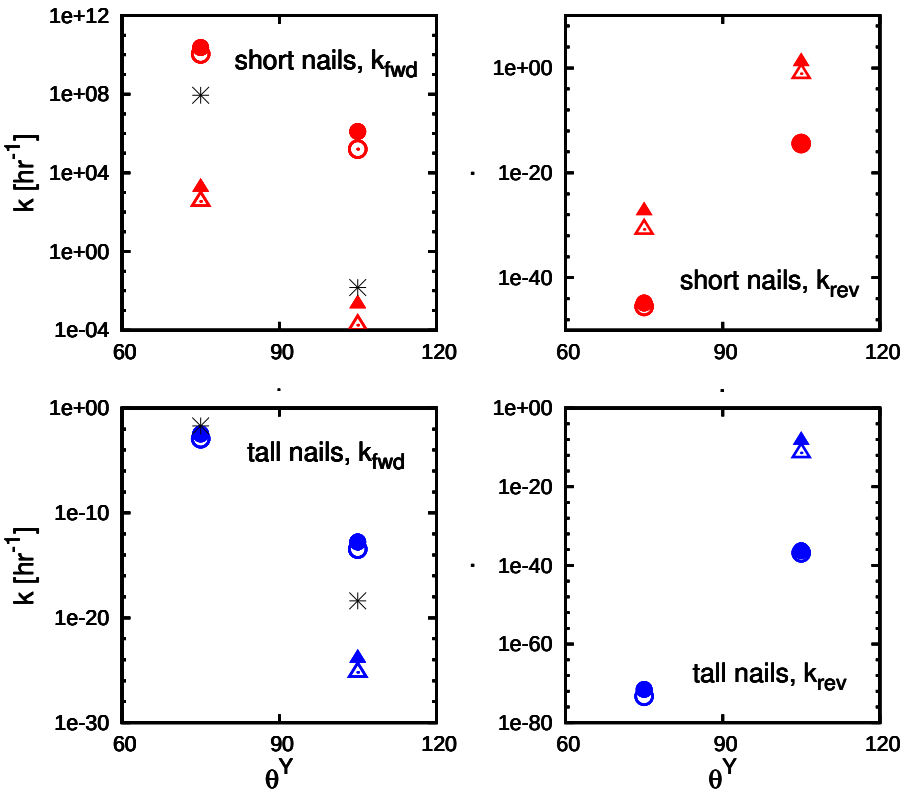

Figure 2.9: Left: Forward (composite-to-wetted) transition rates. Right: Reverse (wetted-to-composite) transition rates. Top: short nails; Bottom: tall nails. In all plots, filled symbols show AXD rates, open symbols show KME rates. Circles are for the droplet and triangles are for the bulk system. Stars show k_{fwd} computed from FFS [32]. Estimated error bars are about equal to symbol size.

the FFS rates (which do not require a Markovian walk over the λ space) are the more accurate, as described earlier. The fact that the BXD rates are higher may suggest that inter-box transitions are not fully Markovian as the BXD-AXD rate estimation requires; i.e., a thorough sampling of degrees of freedom orthogonal to λ is not achieved. The consistent trends with nail height and chemistry support our qualitative conclusions arrived at earlier from FFS wetting rates. Note that FFS dewetting rates are not available for comparison with BXD rates.

2.6 Conclusions

We used a suitably modified version of the BXD method for exploring the free energy landscape of oily droplets on a rough surface. The size of the droplets and protrusions in our simulations is on the order of tens of nanometers, which is one order of magnitude smaller than typical small oily droplets [23] and currently manufacturable features. The length scale of the simulations is hence sufficiently close to real systems of interest that simulated behavior trends are expected to extrapolate semi-quantitatively to realizable nanoscale systems.

We identified both composite and wetted low free energy basins as well as the most stable state for a given chemistry and nail height, and evaluated the intervening free energy barrier. We also used a bulk-like fluid setup to eliminate the effect of the contact line. Traversing the full energy landscape between composite and fully wetted, we identified a region of hysteretic behavior (for the particular order parameter used) when the drop is in a partially wetted state. This does not affect the wetting free energy barriers and transition rate; however, the dewetting free energy barrier and rate are likely slightly under- and over-estimated, respectively. Qualitative conclusions regarding free energy barriers and the effect of nail height and chemistry are consistent between the bulk fluid and drop, and are unaffected by the region of hysteretic behavior. A proper choice of the λ order parameter is crucial as it allows obtaining the most meaningful transitional free energy barriers and, for BXD in particular, the best transition rate estimates (via inter-box transitions which are more closely Markovian).

We also introduced a new control method for BXD that is similar to umbrella sampling where the system is kept within a box by making it energetically unfavorable to travel outside the box. This control technique makes it possible to find

the free energy landscape for systems with a steep energy barrier that could not be traversed with simple velocity reversal, and with better computational efficiency. Also, our method of completing several oscillations at once, by selecting starting configurations from an uncorrelated set of configurations around energy basin A, offers an easy way to parallelize the simulations.

As expected, the re-entrant geometry of the nails does create an energy barrier to the wetting transition for all chemistries tested, as compared to the fluid on posts which showed no free energy barrier for the phillic chemistry. On short nails, some phobic drops prefer to be in the wetted state, although the bulk fluid for the same chemistry prefers the composite state. Doubling the height of the nails more than doubles the free energy barrier (ΔG^*_{fwd}) for both phobic and phillic drops and bulk fluid. With increased feature height, dewetting of a phillic fluid also becomes highly irreversible. Phobic drops with $\theta^Y \geq 130^o$, have an extremely large wetting transition free energy barrier, and if forced to wet, they would spontaneously dewet.

The BXD free energy curves show minor, intermediate wetting barriers between metastable wetting states (e.g., filling one vs. two cavities), which are small compared to the barrier between composite and wetted states. The existence of these metastable wetting states is consistent with macroscopic models [24], and become more prevalent with roughness feature height, in agreement with the findings of Dettre et al. [19]. Based on previously reported FFS transition rates for different drop sizes [32], there is also expected to be some dependence on drop size relative to roughness feature spacing, as wetting is a competition between the drop deforming to reach the bottom of the cavity and spreading on top of nails.

The BXD analysis of the free energy barriers confirms that re-entrant geometry and feature height are effective ways to promote non-wetting, and also that once

the phillic fluid wets, the transition is essentially irreversible.

2.7 Appendix: Simulation details

2.7.1 Quantifying LJ units

We evaluate the energy scale, ϵ, by comparing the critical temperature of tridecane ($T_c = 676$K)[17] to that for a fully flexible LJ fluid of tetramers ($T_c^* = 2.2$)[3], which gives $\epsilon = 4.24 \times 10^{-21}$ J.

The length scale, σ, is found from properties of tridecane ($M = 184.361$ g/mol, $\rho = 0.7564$ g/cm^3 $= 4.1 \times 10^{-3}$ mol/cm^3)[17], a typical alkane. Comparing again to the density of the LJ fluid of tetramers ($\rho = 0.8554$ monomers/σ^3 $= 3.55 \times 10^{-25}$ mol/σ^3 at $T = 1.0$)[3] gives $\sigma = 0.44$ nm.

Next the temperature-dependent surface tension (γ) of tridecane was compared to that from the LJ tetramer fluid [3] at various values of r_c. The best match is for $r_c = 3\sigma$, where $\gamma \approx 19$ mN/m at 370K for both tridecane and the LJ fluid, and the temperature dependence is similar.

We can also evaluate the time unit, τ, as follows (Note that m is the mass of 1 bead):

$$\tau = \sigma\sqrt{m/\epsilon} = 4.2 \times 10^{-10} \text{ m} \left(\frac{7.6 \times 10^{-26} \text{ kg}}{4.24 \times 10^{-21} \text{ J}} \right) = 1.8 \text{ ps} \tag{2.9}$$

The default timestep of 0.005τ is then ≈ 9 fs.

2.7.2 Constraining the system within a box

As in our previous study [32], we define movement of the system between basins according to the fraction of particles that is below the surface, where the surface is taken to be the plane defined by the tops of the nail or post heads. This reaction coordinate will define our box boundaries. In the original BXD method, when the system hits a box boundary, it is kept within the current box by reversing velocities of particles along the reaction coordinate. Our preliminary simulations indicated, however, that this method was not very robust and its performance was very sensitive to, e.g., the amount of thermostatting action employed. While we use this method of control as a reference (see Appendix for a comparison), we adopted a control technique more similar to the soft wall restraining potentials reported by Maragliano et al. [25]. Similar to umbrella sampling, we add a term to the potential when the system travels outside a box, such that it becomes energetically unfavorable to do so. In order to implement this, the order parameter, λ, should be a continuous function. We use the fraction of particles below the surface

$$\lambda = \frac{n}{N} \tag{2.10}$$

where N is the total number of particles in the system, and n is an effective number of droplet particles below the surface

$$n = \sum_{j=1}^{N} f(y_j) \tag{2.11}$$

$$\begin{aligned} f(y_j) &= 0 && \text{for } y_j > y_0 \\ f(y_j) &= 3p^2 - 2p^3 && \text{for } (y_0 - b) < y_j < y_0 \\ f(y_j) &= 1 && \text{for } y_j < (y_0 - b) \end{aligned} \tag{2.12}$$

where $3p^2 - 2p^3$ is chosen to give a continuous function between $f(y_j) = 0$ and $f(y_j) = 1$, $p = (y_0 - y_j)/b$, y_0 is the top of the nail surface, and b is a parameter approximately the size of a particle and is set to 1 σ. The extra potential term, $V(n)$, is zero within the box, and grows rapidly outside the box at either boundary (see Figure 2.10):

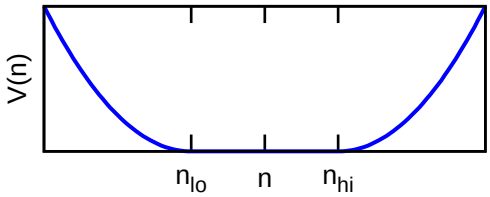

Figure 2.10: Extra potential added as system moves outside the current box of interest

$$\begin{aligned} V(n) &= c(n - n_{lo})^2 && \text{for } n < n_{lo} \\ V(n) &= 0 && \text{for } n_{lo} \leq n \leq n_{hi} \\ V(n) &= c(n - n_{hi})^2 && \text{for } n > n_{hi} \end{aligned} \tag{2.13}$$

where c is a tunable parameter set to 0.1 for the results presented here. The additional force, $-\nabla V(n)$, applied to particles due to $V(n)$ is

$$-\nabla V(n) = -\sum_{j=1}^{N} \frac{\partial V(n_j)}{\partial y_j} = -\frac{\partial V(n)}{\partial n} \sum_{j=1}^{N} \frac{\partial n_j}{\partial y_j} \tag{2.14}$$

where

$$\begin{aligned} \frac{\partial V(n)}{\partial n} &= 2c(n - N\lambda_{lo}) && \text{for } n < N\lambda_{lo} \\ \frac{\partial V(n)}{\partial n} &= 0 && \text{for } N\lambda_{lo} \leq n \leq N\lambda_{hi} \\ \frac{\partial V(n)}{\partial n} &= 2c(n - N\lambda_{hi}) && \text{for } n > N\lambda_{hi} \end{aligned} \tag{2.15}$$

and

$$\begin{aligned}
\frac{\partial n_j}{\partial y_j} &= 0 && \text{for } y_j > y_0 \\
\frac{\partial n_j}{\partial y_j} &= \frac{6}{b^2}(-y_0 + y_j) + \frac{6}{b^3}(y_0^2 - 2y_0 y_j + y_j^2) && \text{for } (y_0 - b) \leq y_j \leq y_0 \\
\frac{\partial n_j}{\partial y_j} &= 0 && \text{for } y_j < (y_0 - b)
\end{aligned} \tag{2.16}$$

2.7.3 Comparing statistics from BXD and a long brute-force MD run

The method used to keep the drop within a box; i.e., either the velocity reversal or the umbrella potential, should not disrupt the normal dynamics of the system. The configurational space sampling within each box should be the same as that in one long MD run. For each method we compare the frequency histograms within a box close to basin A to a long (8×10^7 timesteps) MD run. In these BXD runs, the minimum number of hits at each box boundary is 500 to allow sufficient data points. This corresponds to 8×10^6 timesteps within the box of interest. As Figure 2.11 shows, the different histograms show good agreement, indicating that the control method does not unduly perturb the natural dynamics of the system.

2.7.4 Effect of box spacing

As the boxes get closer together, the simulation time is reduced. However, the boxes must be far enough apart that the spacing doesn't change the results. For example, if they are too close together the transition from one to the next will be easier and the free energy barriers may be artificially reduced. Narrow boxes may

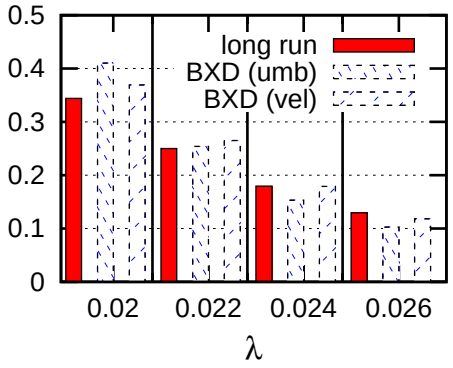

Figure 2.11: Histograms of order parameter coverage for BXD stats within one box vs. long MD run. Solid red boxes: long MD run; cross-hatches: BXD with umbrella control; diagonal lines: BXD with full velocity reversal

also not allow the system to properly sample all relevant configurational degrees of freedom (orthogonal to λ) to obtain converged free energies.

For one case ($\theta^Y = 105^o$), two box spacings were used: $\Delta\lambda = \{0.01, 0.02\}$. The free energy curves are virtually identical, indicating that the closer box spacing is still sufficiently wide enough. The simulation time, which is on the order of 7 days on 1 CPU (10^7 timesteps) for $\Delta\lambda = 0.01$, is ≈ 5 times longer using the wider boxes. Because there is good agreement using the two spacings, the closer spacing ($\Delta\lambda = 0.01$) was used in all remaining simulations.

2.7.5 Free energy barrier via raining

Koishi et al. [20] describe another method to find the free energy barrier of transition from the wetted to composite state, whereby the fluid drop is initially positioned at some distance above the surface, and then moved toward the surface with some fixed velocity, v_d. This is repeated many times with different starting configurations, and for a range of velocities. They suggest the following relation

between the free energy and the probability of transitioning to the wetted state (P_w)

$$P_w = P_0 \ \exp\left(-\frac{\Delta G^*_{\text{fwd}}}{e_k}\right) \tag{2.17}$$

where

$$e_k = \frac{1}{2} m_w v^2 \tag{2.18}$$

This method gives $\Delta G^*_{\text{fwd}} \approx 0.1$ to 1 kT on the short and tall nails with phobic and phillic chemistries, which is 1-2 orders of magnitude too low.

We also attempted to find ΔG^*_{fwd} from a modified version of Koishi's raining method, based on thermodynamic arguments. We start by assuming that at equilibrium

$$P_w = P_0 \ \exp\left(-\frac{\Delta G^*_{\text{fwd}}}{kT_0}\right) \tag{2.19}$$

and that the imposed velocity is effectively adding kinetic energy, thereby changing the temperature such that

$$P_w = P_0 \ \exp\left(-\frac{\Delta G^*_{\text{fwd}}}{kT_0 + \frac{m}{N_f} v_d^2}\right) \tag{2.20}$$

where $N_f = 3$ is the number of translational degrees of freedom per molecule. As this method is correct in the limit as $v_d \to 0$, we restricted our set of velocities to smaller values which give $P_w \leq 0.25$, and also required that at least 10 runs transitioned to the Wenzel state for each velocity point. This method gives $\Delta G^*_{\text{fwd}} \approx 30 - 35$ kT for both phillic and phobic chemistries on short and tall

nails, which is the right order of magnitude, but the value varies between $30 - 70$ kT depending on the sampling of P_w data.

2.7.6 Nomenclature

Symbol	Meaning
b, c	parameters for system constraint
$\mathrm{G}(\lambda)$	free energy profile along entire reaction coordinate
ΔG	thermodynamic free energy difference between basins A and B
$\Delta G^*_{\mathrm{fwd}}$	wetting free energy barrier
$\Delta G^*_{\mathrm{rev}}$	dewetting free energy barrier
$\Delta G_{n-1,n}$	free energy difference between boxes
ΔG_n	free energy difference with respect to some arbitrary zero
$h_{m,m-1}$	number of times the system hits a box wall
$k_{m,m-1}$	forward box-to-box rate coefficients
$k_{m-1,m}$	reverse box-to-box rate coefficients
k_{fwd}	wetting transition rate
k_{rev}	dewetting transition rate
k_{AXD}	transition rate computed by AXD
k_B	Boltzmann constant
K	energy constant in FENE potential
$K_{n-1,n}$	equilibrium constant between neighboring boxes n and $n-1$
m	number of intervals between basin A and B
n	box number, and effective number of particles below the system
N	number of fluid particles

Continued on next page

Nomenclature – continued from previous page

Symbol	**Meaning**
$p(\lambda)$	normalized probability distribution along entire reaction coordinate
p_n	probability of the system residing within each box
$p_n(\lambda)$	probability that reaction coordinate has some value λ within box n
P^{CORR}	correction factor used in AXD method
P_w	probability of transitioning to wetted state in raining method [20]
r	separation between particles
r^*	reduced separation between particles
R_0	maximum extent of FENE bond
t_m	amount of time system spends within box bounded by λ_m and λ_{m-1}
T	system temperature
T^*	reduced system temperature
V	potential energy of system
ϵ	LJ potential well depth and system energy scale
$\Delta\Gamma$	products portion of phase space in AXD method
Γ_1, Γ_2	phase space divisions of reactants used to find AXD transition rate
λ	order parameter, fraction of particle below top of nail plate
λ_m	order parameter value at box edges
λ_{TS}	value of order parameter at transition state for AXD method
σ	minimum separation distance between particles

Continued on next page

Nomenclature – continued from previous page

Symbol	Meaning
	and system length scale
θ	contact angle
θ^Y	Young's (intrinsic) contact angle
τ	system time scale

Bibliography

[1] A Ahuja, J A Taylor, V Lifton, A A Sidorenko, T R Salamon, E J Lobaton, P Kolodner, and T N Krupenkin. Nanonails: A simple geometrical approach to electrically tunable superlyophobic surfaces. *Langmuir*, 24:9–14, 2008.

[2] Rosaline J Allen, Daan Frenkel, and Pieter Rein ten Wolde. Simulating rare events in equilibrium or nonequilibrium stochastic systems. *J. Chem. Phys.*, 124:024102, 2006.

[3] Felipe J Blas, Luid G MacDowell, Enrique de Miguel, and George Jackson. Vapor-liquid interfacial properties of fully flexible lennard-jones chains. *Journal of Chemical Physics*, 129:144703, 2008.

[4] Ernesto E. Borrero and Fernando A. Escobedo. Simulating the kinetics and thermodynamics of transitions via forward flux/umbrella sampling. *J. Phys. Chem. B.*, 113:6434–6445, 2009.

[5] A B D Cassie and S Baxter. Wettability of porous surfaces. *Transactions of the Faraday Society*, 40:546–551, 1944.

[6] David Chandler. Statistical mechanics of isomerization dynamics in liquids and the transition state approximation. *J. Chem. Phys.*, 68:2959–2970, 1978.

[7] Jaroslaw Drelich, Emil Chibowski, Dennis Desheng Mengb, and Konrad Terpilowski. Hydrophilic and superhydrophilic surfaces and materials. *Soft Matter*, 7:9804–9828, 2011.

[8] Fernando A. Escobedo and Francisco J. Martinez-Veracoechea. Optimization of expanded ensemble methods. *J. Chem. Phys.*, 129:154107, 2008.

[9] C W Extrand. Modeling of ultralyophobicity: Suspension of liquid drops by a single asperity. *Langmuir*, 21:10370–10374, 2005.

[10] Daan Frenkel and Berend Smit. *Understanding Molecular Simulation*. Academic Press, second edition, 2002.

[11] Alberto Giacomello, Simone Meloni, Mauro Chinappi, and Carlo Massimo Casciola. Cassie-baxter and wenzel states on a nanostructured surface: phase diagram, metastabilities, and transition mechanism by atomistic free energy calculations. *Langmuir*, 28:10764–10772, 2012.

[12] David R Glowacki, Emanuele Paci, and Dmitrii V Shalashilin. Boxed molecular dynamics: A simple and general technique for accelerating rare event kinetics and mapping free energy in large molecular systems. *Journal of Physical Chemistry B*, 113:16603–16611, 2009.

[13] David R Glowacki, Emanuele Paci, and Dmitrii V Shalashilin. Boxed molecular dynamics: Decorrelation time scales and the kinetic master equation. *Journal of Chemical Theory and Computation*, 7:1244–1252, 2011.

[14] Gary S. Grest, David R. Heine, and Edmund B. Webb III. Liquid nanodroplets spreading on chemically patterned surfaces. *Langmuir*, 22:4745–4749, 2006.

[15] Eric M. Grzelak and Jeffrey R. Errington. Nanoscale limit to the applicability of wenzel's equation. *Langmuir*, 26:13297–13304, 2010.

[16] Eric M. Grzelak, Vincent K. Shen, and Jeffrey R. Errington. Molecular simulation study of anisotropic wetting. *Langmuir*, 26:8274–8281, 2010.

[17] William M Haynes, editor. *CRC Handbook of Chemistry and Physics*. CRC, 91st edition, 2010.

[18] Stephan Herminghaus, Martin Brinkmann, and Ralf Seemann. Wetting and dewetting of complex surface geometries. *Annu. Rev. Mater. Res.*, 38:101–121, 2008.

[19] R E Johnson and R H Dettre. Contact angle, wettability and adhesion. *Adv. Chem. Ser.*, 43:112–135, 1964.

[20] Takahiro Koishi, Kenji Yasuoka, Shigenori Fujikawa, Toshikazu Ebisuzaki, and Xiao Cheng Zeng. Coexistence and transition between cassie and wenzel state on pillared hydrophobic surface. *PNAS*, 106:8435–8440, 2009.

[21] Kurt Kremer and Gary Grest. Dynamics of entangled linear polymer melts: A molecular-dynamics simulation. *Journal of Chemical Physics*, 92:5057–5086, 1990.

[22] Vaibhaw Kumar, Shyam Sridhar, and Jeffrey Errington. Monte carlo simulation strategies for computing the wetting properties of fluids at geometrically rough surfaces. *J. Chem. Phys.*, 135:184702, 2011.

[23] Jennifer Labs and Terry Parker. Diesel fuel spray droplet sizes and volume fractions from the region 25 mm below the orifice. *Atomization and Sprays*, 13:45–62, 2003.

[24] J. Long and P. Chen. On the role of energy barriers in determining contact angle hysteresis. *Adv. Coll. Interf. Sci.*, 127:55–66, 2006.

[25] Luca Maragliano, Eric Vanden-Eijnden, and Benoit Roux. Free energy and kinetics of conformational transitions from voronoi tessellated milestoning with restraining potentials. *J. Chem. Theory Comput.*, 5:2589–2594, 2009.

[26] Abraham Marmur. Wetting on hydrophobic rough surfaces: To be heterogeneous or not to be? *Langmuir*, 19:8343–8348, 2003.

[27] Daniele Moroni, Titus S. van Erp, and Peter G. Bolhuis. Simultaneous computation of free energies and kinetics of rare events. *Phys. Rev. E*, 71:056709, 2005.

[28] M Nosonovsky. Multiscale roughness and stability of superhydrophobic biomimetic interfaces. *Langmuir*, 23:3157–3161, 2007.

[29] M Nosonovsky and B Bhushan. Stochastic model for metastable wetting of roughness-induced superhydrophobic surfaces. *Microsystem Technologies*, 12(3):231–237, 2006.

[30] Neelesh A Patankar. Transition between superhydrophobic states on rough surfaces. *Langmuir*, 20(17):7097–7102, 2004.

[31] S. Plimpton. Fast Parallel Algorithms for Short-Range Molecular Dynam-

ics (http://lammps.sandia.gov). *Journal of Computational Physics*, 117:1–19, 1995.

[32] Elizabeth S Savoy and Fernando A Escobedo. Molecular simulations of wetting of a rough surface by an oily fluid: Effect of topology, chemistry and droplet size on wetting transition rates. *Langmuir*, 28:3412–3419, 2012.

[33] T. Schneider and E. Stoll. Molecular-dynamics study of a three-dimensional one-component model for distortive phase transitions. *Phys. Rev. B.*, 17:1302–1322, 1978.

[34] Anish Tuteja, Wonjae Choi, Minglin Ma, Joesph M Mabry, Sarah A Mazzella, Gregory C Rutledge, Gareth H McKinley, and Robert E Cohen. Designing superoleophobic surfaces. *Science*, 318:1618–1622, 2007.

[35] Anish Tuteja, Wonjae Choi, Gareth H McKinley, Robert E Cohen, and Michael F Rubner. Design parameters for superhydrophobicity and superoleophobicity. *MRS Bulletin*, 33:752–758, 2008.

[36] Chantal Valeriani, Rosalind J. Allen, Marco J. Morelli, Daan Frenkel, and Pieter Rein ten Wolde. Computing stationary distributions in equilibrium and nonequilibrium systems with forward flux sampling. *J. Chem. Phys.*, 127:114109–114111, 2007.

[37] Titus S. van Erp and Peter G. Bolhuis. Elaborating transition interface sampling methods. *J. Comp. Phys.*, 205:157–181, 2005.

[38] Eric Vanden-Eijnden and Maddalena Venturoli. Exact rate calculations by trajectory parallelization and tilting. *J. Chem. Phys.*, 131:044120, 2009.

[39] Eric Vanden-Eijnden and Maddalena Venturoli. Markovian milestoning with voronoi tessellations. *J. Chem. Phys.*, 130:194101, 2009.

[40] R N Wenzel. Resistance of solid surfaces to wetting by water. *Industrial and Engineering Chemistry*, 28:988–994, 1936.

[41] Hongfei Wu, Ali Borhan, and Kristen A. Fichthorn. Coarse-grained interaction of a fluid with a physically-patterned solid surface: Application to nanodroplet wetting. *J. Low Temp. Phys.*, 157:277–295, 2009.

[42] Thomas Young. An essay on the cohesion of fluids. *Philosophical Transactions of the Royal Society of London*, 95:65–87, 1805.

[43] Yabin Zhang, Yu Chen, Lei Shi, Jing Li, and Zhiguang Guo. Recent progress of double-structural and functional materials with special wettability. *J. Mater. Chem.*, 22:799–815, 2012.

CHAPTER 3

MOLECULAR SIMULATION OF THE EFFECTS OF HUMIDITY AND OF INTERFACIAL SI– AND B–HYDROXYLS ON THE ADHESION ENERGY BETWEEN GLASS PLATES*

3.1 Abstract

Adhesion energies can be reasonably quantified with macro-scale theoretical treatments for millimeter-size particles and above, but not so for sub-micron length scales where heterogeneities in surface morphology and chemistry play a significant role. Measurements of adhesion are also known to vary by an order of magnitude or more. Atomistic scale modeling has been used previously to quantify adhesion energies in wet environments for pure silica surfaces based on several interaction potentials specific to silica and water. To extend such modeling to more complex glass materials, we adopt an amorphous glass potential which has been parameterized for many species, and use a simplified approach to develop interaction parameters between the hydroxylated surface and SPC/E water. Using these interface parameters we compute adhesion energies for pure SiO_2, and 90 mol % SiO_2 + 10 mol % B_2O_3, in dry and humid conditions. We find that the addition of B_2O_3 reduces adhesion, due to both the lower affinity of the B-hydroxyl for water as compared to the Si-hydroxyl, and also due to changes in the bulk structure, both of which reduce hydrogen bonding. The condition of lowest adhesion for pure silica occurs in a fully hydroxylated surface at low relative humidity (RH),

* Reprinted with permission from Escobedo, F. A.; An article on this work is currently under review with *Langmuir*.

whereas for the SiO_2 + B_2O_3 surface it occurs in a dry environment. At high RH, the water between the plates forms a clear liquid bridge, with expected wetting angle at the water-surface interface due to surface tension, whereas at the lowest RH, the water connects in chains of hydrogen bonded molecules that form and break during the adhesion process, so that capillary forces do not come into play. The adhesion energy trends are qualitatively consistent with the extent of wetting on each surface.

3.2 Introduction

The use of silicate glass materials is ubiquitous in many industries including laboratory and consumer products, pharmaceuticals, and environmental applications. Understanding and controlling adhesion between glass surfaces is important, for example, in the manufacture of some labware (like multi-well plates), glass panels for automotive or architectural applications, and glass screens for consumer products like computers, tablets, and TVs. The relevant length scales which determine performance are becoming ever smaller as fabrication of micro and nanoscale devices is achievable. For many applications, understanding the interfacial behavior is key to improving quality and performance. At such small length scales, capillary forces can have significant impact on how surfaces interact. The existence of numerous interaction potentials devoted specifically to describing the interaction of silica and water underscores this fact [5, 8, 11, 17, 18, 21, 24, 27, 28].

Adhesive energy is a characteristic interfacial property which can be approximated using theories based on the Young-Laplace and Kelvin equations and assuming the particle has some ideal shape, such as a sphere, cylinder or cone [14],

and that the surface is either another particle or a flat surface, either smooth or with some specific roughness [19]. The computed adhesion values depend heavily on these factors as well as empirical quantities such as a Hamaker coefficient which can be off by several orders of magnitude due to assumptions about particle-surface geometry [1], and do not capture local variations on the surface. While these approximations are generally considered reasonable at length scales of tens of microns and above [16], we are interested in how local variations in composition and the presence of water will affect adhesive behavior.

Adhesion can be measured experimentally by atomic force microscopy (AFM) where, for example, a pyramid-shaped glass tip at the end of a cantilever arm is brought into contact with a surface and the force to remove the tip is computed based on a spring constant [6]. In some cases a glass shard is attached to the end of the tip [9]. Adhesion values measured this way vary by a factor of 2 to 10 [7] and depend heavily on assumptions about the tip size and the radius of curvature, which will change the contact surface area, and which can change sometimes dramatically over a series of measurements as the tip is worn down.

Published experimental and simulation results show varying dependence of adhesion on relative humidity, including monotonically increasing [9], increasing to a plateau [25, 33], and running through a maximum at intermediate RH values [7, 16]. In some simulation studies the adhesive force vanishes with dry surfaces [5, 20].

Molecular dynamics simulations have been used previously to compute the adhesion energy between silica surfaces and particles in the presence of varying amounts of water corresponding to a range of relative humidities [5, 15, 16]. These works give a baseline of comparison for our study, where we compare the behavior

for our fully hydroxylated pure silica system and then extend to a composition containing B_2O_3, as well as pure silica with reduced amount of surface hydroxylation. In this way, we hope to gain insight about how the isolated effects of composition and surface energy influence adhesion. We use the Pedone force field [22] to describe our bulk material because it is a fairly simple, non-bonded potential which accurately predicts many bulk structural properties of amorphous glass materials and includes parameters for many typical glass components. Using methods similar to those used by Hassanali et. al. to extend the BKS potential [11], and by Cole and Payne for a Stillinger-Weber based potential [5], we use density functional theory (DFT) energies to estimate Lennard-Jones parameters between each hydroxyl type and SPC/E water [3]. Using these parameters we study the wetting and adhesion behavior of surfaces of both compositions under several levels of relative humidity ranging from dry to fully saturated.

There are numerous models to describe the water-silica interaction [5, 8, 11, 17, 18, 21, 24], many of which use complicated three-body terms, correction terms, chemical bonding, polarization, or other effects that make them not transferable to systems other than silica and water. We selected the Pedone potential and a compatible, simplified interaction potential for the hydroxylated surface with water in hopes that the comprehensive set of Pedone potential parameters can be leveraged to make this approach extensible to adhesion studies of more complex bulk compositions.

The remainder of this article is organized as follows: In the Methods section we describe the computational details of the simulated systems, hydroxylation of surfaces, development of the potential between the hydroxylated glass surface and water, and how we compute the adhesion energies. In the Results and Discus-

sion section we analyze the wetting and adhesion behavior we computed for each condition and compare to available published results, and discuss the effect of hydrogen bonding and affinity for water. In the last section we present our concluding remarks.

3.3 Methods

Creating the systems. We consider two compositions of amorphous material: one pure SiO_2 and one with 10 mol % B_2O_3. The surface hydroxylation was selected to represent a nearly fully hydroxylated surface (3.0 OH/nm^2) as well as two lower density (0.7 and 1.5 OH/nm^2), more energetic surfaces. Each system is created by first simulating a bulk mixture of the relevant oxides, then making two surfaces by cleaving the bulk and equilibrating, hydroxylating the surfaces, and finally adding water between the surfaces. Each of these steps is described in more detail below.

The bulk glass structure is created through a series of molecular dynamics (MD) and Metropolis Monte Carlo (MC) steps, as the glass is annealed from 4000^{o}C down to 300^{o}C in steps of 200^{o}C, with a final step of 100^{o}C. This combination of MD and MC runs while quenching has been shown to be an efficient and accurate process for creating atomistic glass structures [31]. At each temperature step the system is run for 4×10^5 MD steps of 0.001 ps at constant temperature, followed by 2×10^7 trial moves with an acceptance ratio of 0.35 in constant pressure MC. The starting locations of O, Si and B atoms are random within a cubic periodic simulation box, with the number of each type of atom defined by the desired molar concentrations, and the simulation box size defined by the estimated final density (2.4 g/cc, based

on SiO_2). The MD runs of the anneal cycle are performed using the NVT ensemble in GROMACS [12], and an in-house program is used for the MC portion. A final NPT step is used to relax the structure. In the final structure, bond lengths and coordination numbers are compared to known values. This process is described in more detail elsewhere [31].

The pure silica system has 5001 atoms (1667 Si and 3334 O) and the equilibrated cubic system is 41.3 Å per side. The borosilicate system has 5440 atoms (1688 Si, 376 B and 3376 O), and measures 42.95 Å per side. These sizes are for the final equilibrated bulk systems (before cleaving, hydroxylating and duplicating).

The remainder of the MD simulations are performed using LAMMPS [23], in the NVT ensemble at 300K using a Nose-Hoover thermostat with a damping parameter of 0.018 timesteps, unless otherwise noted. For each system, two surfaces are created by opening the periodic boundary conditions in the z-dimension, and exposing the glass at those boundaries to a vacuum. The x and y dimensions do not change. In the z dimension the length is fixed at 140 Å and the slab option is used to properly handle calculations of the long-range interactions, which are solved using PPPM with accuracy of 10^{-7} and order 7. The system is allowed to equilibrate until the energy stops changing. Surfaces created in this way have only molecular scale roughness, and high energy due to dangling bonds, some of which heal upon equilibration. The resulting structure has low valence atoms near the surfaces, which are satisfied through hydroxylation.

The bond valence, v, of any atom i in the system is computed to identify low-valence atoms near the surface using the formula

$$v_i = \sum_i \exp\left(\frac{R_0 - R_i}{b}\right) \tag{3.1}$$

where R_0 is the nominal bond length (1.62 Å and 1.37 Å for Si-O and B-O, respectively [4]), b=0.37 is an empirical constant[4], and R_i is the distance to all other ions in the system with the opposite sign (e.g. anions if computing v_i for a cation).

A majority of the bond valence values, before hydroxylation, are clustered around the expected coordination (2 for oxygen, 4 for silicon; 3 for boron), but near the top and bottom surfaces there are low valence atoms (see Figure S1 in the Supporting Information). These are the ones selected for hydroxylation, meaning that an H is added to the selected O atoms, and an OH is added to the selected cations. The surface atoms with the lowest v_i values are selected first, and the same number of O and cations are hydroxylated per surface in order to maintain a charge balanced system.

The rules for adding H and OH atoms are as follows: An O is added to Si at a distance of R_0, equidistant from the closest 3 O atoms, and in the direction outward from the surface. An H is added to an O at a distance of 1 Å, outward from the surface, and with a Si–O–H bond angle of 109.5^o. This procedure is performed iteratively, adding approximately 5 H/OH pairs each time, and running an NVT MD simulation between each round to allow the system to relax. This continues until a desired density of OH on the surface is reached, where that density is found by counting all O–H bonds and dividing by the projected surface area. The same procedure is used to hydroxylate the SiO_2 + B_2O_3 system, with the added constraint that the relative number of each type of cation at the surface is

approximately equal to the bulk distribution. The B–O–H hydroxylation angle is 120.0^o, in accordance with the 3-coordination state of the B in the bulk.

Both surfaces after hydroxylation have atomistic roughness of approximately 1.5 Å (estimated using the z-coordinate of all atoms within 4 Å of the vacuum above the surface as $\sqrt{(1/n)\sum_{i=1}^{n}(z_i - \overline{z})^2}$), which is in the range of roughness values reported for polished and treated SiO_2 surfaces [17], and the surfaces consist of regions of hydrophilic and hydrophobic character, depending on the local hydroxyl density.

After hydroxylating the surface, the bulk system is duplicated such that the two different surfaces are facing each other. A thick (20-30 Å) layer of SPC/E water is added as a block between the two surfaces. The far outer hydroxylated surfaces are in vacuum. This system of vacuum-glass-water-glass-vacuum is allowed to equilibrate in the NVT ensemble, using velocity rescaling for temperature control at 300 K, until the energy stops changing (600 ps). Velocity rescaling is used here because we don't need to know the dynamics during equilibration, and we do want to remove z-oscillations that can occur as the water and surface come into contact and relax. The system is then run for an additional 400 ps, and snapshots are stored every 5000 timesteps (1 ps) and used to study axial density profiles and radial distribution functions of the equilibrated glass-water systems.

Using the final equilibrated structures, slabs are extracted with a specific amount of water molecules, corresponding to 0 – 2 monolayers [ML] of water (see Table 3.2) which will be used to perform adhesion energy simulations as described in the next section. This range of water volumes span conditions from low relative humidity up to saturated conditions. The relative humidity is estimated from water adsorption isotherms presented in Reference [15]. Several grand canonical

Monte Carlo simulations of water adsorption on our fully hydroxylated silica surface (results not shown) confirmed that this is a reasonable estimate of relative humidity. Starting configurations of bulk glass plus a water layer are extracted from both sides of the bulk water. The underlying surfaces that will be approaching each other have slightly different roughness and composition, although the bulk composition and hydroxyl density are the same for a given system. For the dry, hydroxylated surfaces, it is expected that the alignment of roughness features and hydroxyls on the surfaces approaching each other will have noticeable impact on the adhesion energy [16], and therefore, four separate simulations are done for these cases and the average adhesion energy plus standard deviation is reported. The four cases correspond to rotations of the starting position of the top slab by 0, 90, 180 and 270 degrees around the z axis, which is normal to the surfaces.

Interaction potentials. Pairwise interactions within the amorphous glass material are described by the Pedone potential [22] which has been shown to accurately represent the polymorphs of amorphous glass and silica and has been parametrized for a large number of oxides, potentially allowing the extension of the current methods to the study of more complex glass compositions. The potential energy has the form:

$$U(r) = \frac{z_i z_j e^2}{r} + D_{ij}[1 - \exp^{-a_{ij}(r-r_0)^2} - 1] - \frac{C_{ij}}{r^{12}} \tag{3.2}$$

where D_{ij}, a_{ij}, r_0 and C_{ij} are tabulated parameters [22], and r the distance between atom pairs. z_i and z_j are partial charges, with the charge on the oxygen fixed at -1.2 and the cations assigned self-consistent charges.

Water is described by the SPC/E model, which is a rigid, non-polarizable water

model and is known to reproduce the structural and dynamical properties of water well. Both the SPC and SPC/E water models have been used to study water in contact with an oxide surface [2, 15] and Ho et. al. showed that for SPC and SPC/E water in contact with silica substrates, no observable differences were reported [13]. The LJ potential values for SPC/E water are $\epsilon = 1.0406$ kJ/mol and $\sigma = 3.6876$Å, and partial charges are $q_O = -0.8476$, $q_H = 0.4238$. The O–H bond length is fixed at 1 Å, and H–O–H bond angle fixed at 109.5^o, both controlled using the SHAKE algorithm within LAMMPS.

To describe interactions at the interface between the glass slab and water, we use a LJ potential and determine the ϵ and σ values by comparing classical MD simulations to DFT calculations for each molecule type. A single water molecule is placed at a fixed distance from a single silicic acid (H_4SiO_4) molecule, with the water oxygen (O^w) pointing towards one of the hydroxyl hydrogens (H^h) on the H_4SiO_4 (see Figure S2 in the Supporting Information). The DFT energy is computed with NWChem [32] using the b3pw91 functional, and starting with 6-31G* as the basis set, then refining with the larger 6-311++G(2d,2p) basis set. The energy is calculated at a series of distances between O^w and H^h to create the potential energy curve shown in Figure S3 (also given as Supporting Information). The same configurations are then run with MD in LAMMPS, using a LJ potential between O^w and H^h. First σ is fixed and then ϵ is varied until the well depth in the classical system's potential energy curve matches the DFT curve. This process was repeated using H_3BO_3 and H_2O. Charges on the surface hydroxyl O and H are fixed at -1.2 and 0.6 to maintain charge neutrality and consistency with the bulk material. For each molecule, two parameter sets of ϵ and σ were identified which match the DFT well depth, and several benchmark evaluations were used to select one set.

For the two values of σ considered, 3.5 and 5.0 Å, the heats of immersion for fully hydroxylated pure silica were 442 and 296 mJ/m^2 (Table 3.2). The latter is closer to the experimental value of 158 mJ/m^2 for silica with an OH density of 3.4/nm^2 [30]. We note, however, that experimental values between 200 and 800 mJ/m^2 have been reported [11], so we are not attempting to match any value accurately, but rather capture the expected trends. The wetting behavior of water on the fully hydroxylated surface was also considered, where the lower σ value allowed the water to completely wet the surface whereas the σ=5 Å parameter set resulted in a water contact angle that was very low but non-zero. The latter is the expected behavior for our surface with 3 OH/nm^2 [33]. Therefore, σ was fixed at 5 Å and the ϵ which gave the desired well depth for each cation was used. With this parameter set we are able to see the wetting behavior change with hydroxyl density (Figure 3.2), going from fully wet on the highest energy (low hydroxyl density) surface, to low contact angle on the fully hydroxylated surface. Note that this behavior is different from what is observed on equilibrated surfaces with different hydroxyl density, where increased hydroxylation leads to increased hydrophillicity [29], because our low hydroxyl-density surfaces represent an intermediate state with high energy oxygen sites that would prefer to react with water and form new hydroxyl groups, such as a freshly fractured surface.

This approach to parameterizing the surface-water interaction is similar to previous work on the silica-water interface [11, 5], and offers a simple non-bonded, non-polarized model which can be easily extended to include other bulk species described by the Pedone potential for more complex glass compositions. In the results section we evaluate the relative impact of the selection of σ and ϵ and show that the values chosen are suitable to make comparisons between the adhesion energies of the different systems. The final potential parameter values for each

species type are shown in Table 3.1, where standard mixing rules ($\epsilon_{ij} = \sqrt{\epsilon_i \epsilon_j}$) were used to determine interactions between different species types.

Species i	Species j	ϵ [eV]
$O^{h,Si}$	O^{w}	0.00007
$O^{h,Si}$	$O^{h,Si}$	0.00007
$O^{h,B}$	O^{w}	0.00014
$O^{h,B}$	$O^{h,B}$	0.00014
$O^{h,Si}$	$O^{h,B}$	0.0001

Table 3.1: LJ ϵ values to describe pairwise interactions between each type of hydroxyl O (O^h) and also their interaction with water O (O^w). For all cases, σ=5.0Å.

Adhesion energy. To estimate the adhesion energy between two slabs, we follow a similar procedure as that described by Leroch et. al. [15]. Two slabs of hydroxylated amorphous material are initially placed 5-15 Å apart (depending on the amount of water present as more water requires a greater distance to allow formation of a liquid bridge between the plates), and moved towards each other in steps of 0.2 Å, equilibrating the system at each displacement step for 100 ps and then running for an additional 200 ps, during which time forces are collected every 2 ps and then averaged to give the mean force acting between the plates A and B at the given z separation [15]

$$F_{AB}(z) = \langle F(z) \rangle = \left\langle \hat{\mathbf{z}} \frac{1}{2} (\vec{F_A} - \vec{F_B}) \right\rangle \tag{3.3}$$

The rate of approach equates to 0.002 Å/ps, which is deemed to be slow enough that the force vs. distance curve can be integrated along z to find the change in free energy, or the potential of mean force (PMF). This was confirmed by running select cases for longer time and not observing change in the mean forces. In the results section we show the mean forces along z and the PMF curve for several

systems under study (Figures 3.3-3.5). The PMF curves are shifted so the fully separated slabs are at zero; in this way the minimum in the PMF curve, which corresponds to the point where the forces on the slabs become repulsive, gives the adhesion energy. After integrating the forces, the values are divided by twice the area of the initial equilibrated bulk system. Note that this is the projected area and does not account for roughness, an assumption which will introduce some small amount of error.

Adhesion energy is computed in this way for dry, hydroxylated slabs, and also with the water layer thicknesses shown in Table 3.2. One difference between our simulations and those of Leroch [15] is that we apply time integration to the first 10 Å of each amorphous slab, as well as to the water and hydroxyls. The remaining slab atoms are fixed, which reduces overall simulation time and also fixes the separation between the slabs.

3.4 Results and Discussion

Wetting of each surface. DFT energies of a water molecule O approaching a donor hydroxyl for each molecule type show that the B-hydroxyl has less affinity for water than the Si-hydroxyl (Figure S3). Note that the well depth is not exactly equal to a binding energy due to the constraints imposed on the water molecule approaching the donor hydroxyl. The Si-hydroxyl forces with water are longer range than the B-hydroxyl forces. We were not able to exactly match the position of the well depth by changing only σ and ϵ. While adjusting charges may result in a closer match, we want to maintain consistent charges throughout. Because we are studying adhesion, the well depth is the more important metric as it will have

greater influence over the attraction of the water to the surface.

Heats of immersion, which are computed from full-system MD simulations of surfaces of each composition in contact with a thick layer of water, are consistent with the potential energy trends indicated above in-so-far as adding B_2O_3 reduces the value by about half (Table 3.2). Note that the heat of immersion did not change much with hydroxylation density on the pure silica system, although it does increase with surface energy, which is expected. While the overall potential energy is lower for the system with fewer hydroxyls, the difference for each when compared with cases with and without the water layer, was approximately the same, resulting in similar heats of immersion.

To test the relative impact of the force field parameters for the hydroxyl-water interaction as compared to the effect of bulk structure with and without B, the heat of immersion was also computed for the SiO_2 + B_2O_3 system using the Si-hydroxyl parameters for the B-hydroxyls. In other words, all interactions in Table 3.1 are equal to the $O^{h,Si}$ – O^{w} interaction. In this modified system the heat of immersion was 208 mJ/m^2, meaning that approximately 1/3 of the difference in heat of immersion between the compositions is due to the force field parameters from the MD to DFT fitting. The rest of the difference is likely due to bulk behavior of the B atoms that is different from the Si atoms, which leads to steric effects that reduce the overall hydrogen bonding between the surface and water. This will be discussed further with respect to adhesion energy results.

Radial distribution functions between hydroxyl and water molecules, and bulk bridging oxygens with water hydrogens, were computed for each of the four systems of hydroxylated slabs equilibrated next to a thick water layer. The first peak in the left and center plots in Figure 3.1 indicate the level of hydrogen bonding between

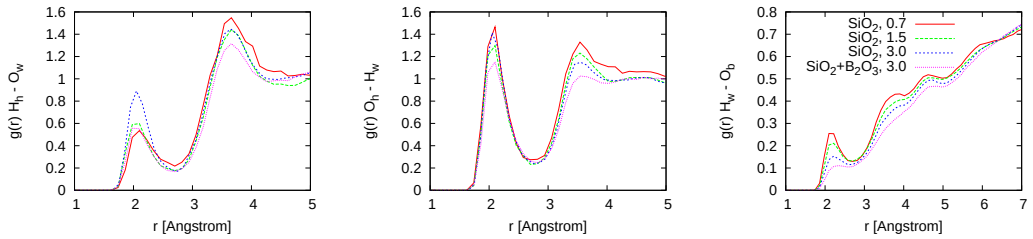

Figure 3.1: Radial distribution functions of hydroxyls with water for each surface. Left: surface hydroxyl hydrogens with water oxygens. Center: surface hydroxyl oxygens with water hydrogens. Right: water hydrogens with bridging oxygens. In the key on the right plot, the value is the surface hydroxyl density.

surface hydroxyls and water molecules. The fact that the first peak, around 2 Å, is higher in the center plot shows that most of the hydrogen bonds are formed between hydroxyl oxygens and water hydrogens, with a lesser amount formed between hydroxyl hydrogens and water oxygens. Comparing the three pure silica surfaces, this difference is more pronounced with lower hydroxylation density. Overall the number of hydrogen bonds is lower for the system with B_2O_3. The right-most plot in Figure 3.1 represents hydrogen bonding between water hydrogens and bridging oxygens in the bulk. Not surprisingly, the first peak shows that the lowest hydroxyl density surface forms the most hydrogen bonds of this type, as the waters are able to get closer to the bulk due to the presence of fewer hydroxyl groups. Additionally, the low hydroxyl density surface is very energetic and hydrophilic. The distributions are most similar to what Leroch found using the Clay forcefield [15], although our hydrogen bonding with the hydroxyl in the donor position is lower. This is likely a result of the hydroxyl groups preferentially orienting parallel to the surface, which is discussed in more detail in the Supplemental Information.

We further explore the wetting behavior by placing a water droplet of 542 molecules ($\approx 1.6 \times 10^{-17} \mu$L) on each hydroxylated surface and equilibrating for a minimum of 1000 ps. Each of the surfaces was copied in the x and y directions to provide a larger surface for the water drop to spread onto, such that the bulk

material contains 4 times the number of atoms of the original bulk systems. The final wetting state for each composition is shown in Figure 3.2. Although we did not evaluate a contact angle (θ) due to the irregular shape of the water drop and overall high degree of wetting, a difference in wetting behavior can be observed which is, again, consistent with the trends of binding energies and heats of immersion. The pure silica is more wetting (lower θ) than the system containing B_2O_3, and the contact angle also decreases with amount of surface hydroxylation such that on the least hydroxylated surface the water fully wets the surface. The water drop on the surface with boron hydroxyls preferentially avoids the B–OH sites.

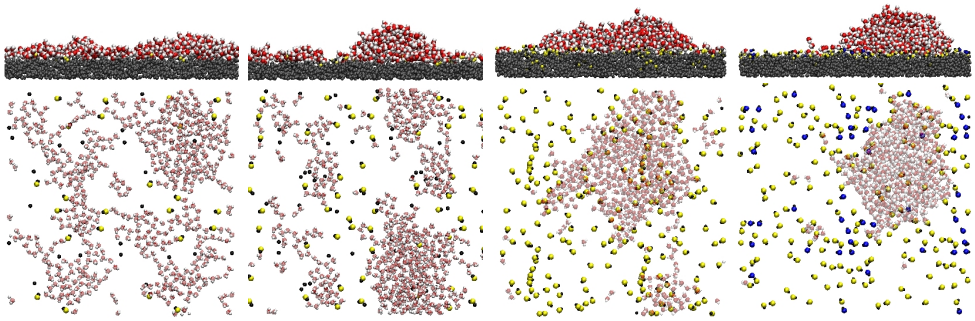

Figure 3.2: Wetting of each surface by SPC/E water. Top row: side view of drop on surface. Bottom row: top-down view of drop on surface, with semi-transparent water molecules and surface hydroxyls only. Hydroxyl oxygen types by color: yellow: Si–OH; blue: B–OH. From left to right: 100% SiO_2: 0.7, 1.5 and 3.0 OH/nm^2, and 90% SiO_2+10% B_2O_3: 3.0 OH/nm^2.

Adhesion energies. Adhesion energies in Table 3.2 were computed for dry and humid conditions. Similar to calculations reported previously by Leroch et. al [15] and Cole et. al. [5] as well as measurements of adhesion energy at silica-silica interfaces [33], the adhesion energy increases with RH to a plateau. We did not look at water levels as high as 3 ML and so no dip in adhesion was observed. At high values of RH the adhesion is independent of the surface and is driven by water interactions, and the adhesion energy remains very close to the surface tension of water, 72 mJ/m^2. Some factors that will influence the adhesion are local

surface roughness, amount of surface hydroxylation, and surface contamination. The results for silica are in the range of acceptable values, as compared to previous simulations [15, 5] and experiment [33].

Bulk comp. [mol%]	Hydroxyl density [OH/nm^2]	Heat of Immersion σ=5(2.5)Å [mJ/m^2]	Amount of water / surface [# monolayers, (%RH), $\mu mol/m^2$]						
			0 (0) *0.0*	**0.17** (4) *3.2*	**0.33** (18) *6.5*	**0.5** (40) *9.7*	**1.0** (82) *19.5*	**1.5** (100) *29.2*	**2.0** (100) *39*
			Adhesion energies [mJ/m^2]						
100% SiO_2	0.7	318	243±35		35	43			
100% SiO_2	1.5	311	130±52		25	35			
100% SiO_2	3.0	296 (442)	37±8	19	26	39	59	77	78
90% SiO_2 10% B_2O_3	3.0	164 (407)	8±6		21	29			

Table 3.2: Heat of immersion and adhesion energies for the four systems simulated. Heat of immersion values are shown for the two hydroxyl – water LJ interaction parameter sets described in the Methods section, as indicated by the σ value. Estimates of RH are taken from Figure 10 of Ref. [15], and the number of monolayers is based on 16 μmol/m^2 ≈1 monolayer = 1 ML (consistent with the volume of water in the first layer indicated by the axial distribution of water molecules on the surface).

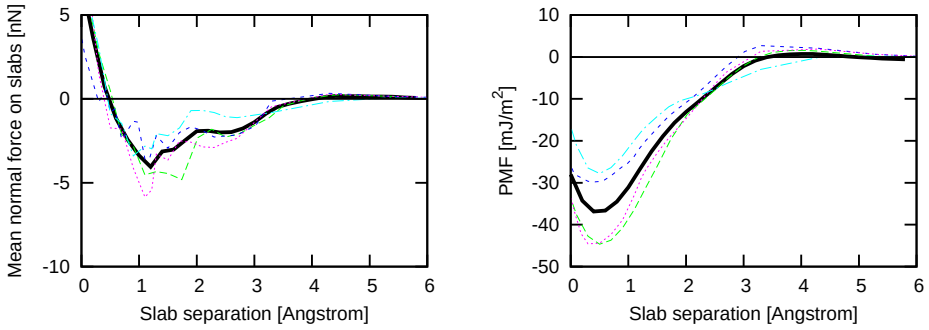

Figure 3.3: Left: Force vs. distance curve for dry hydroxylated (3.0 OH/nm^2) pure silica slabs approaching each other, with four different orientations of the top plate around the normal axis. Right: PMF for the same system. Solid black curve is the average for the four orientations.

Figures 3.3-3.4 and S5-S6 (Supporting Information), show the detailed forces and PMF curves for each of the dry hydroxylated surfaces as a function of separation. For each system there are four curves, each one representing a different

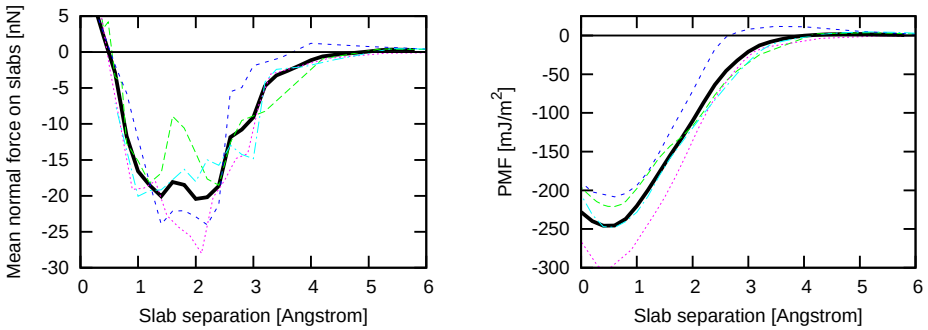

Figure 3.4: Left: Force vs. distance curve for dry hydroxylated (0.7 OH/nm^2) pure silica slabs approaching each other, with four different orientations of the top plate around the normal axis. Right: PMF for the same system. Solid black curve is the average for the four orientations.

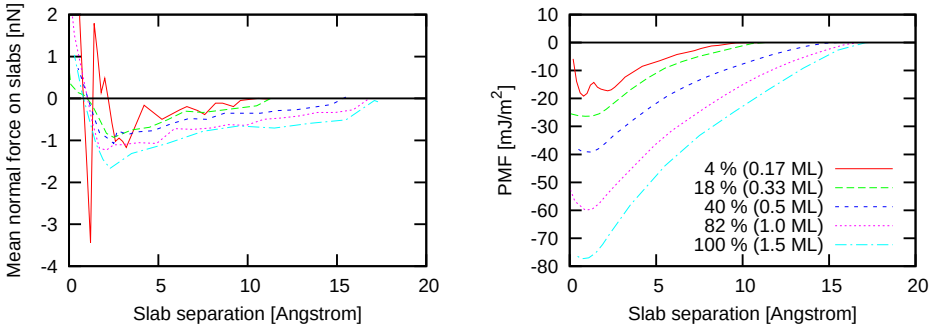

Figure 3.5: Left: Force vs. distance curve for hydroxylated (3.0 OH/nm^2) pure silica slabs approaching each other, with 0.33-2 ML water on each plate at the start. Right: PMF for the same system.

alignment of the surfaces facing each other. This is achieved by fixing the starting configuration of the bottom slab, and rotating the top slab around the z-axis in 90^o increments for the starting configuration of each run. We do this for the dry systems because it is expected that the alignment of the surface roughness features and hydroxyl groups as the slabs approach each other will have a significant impact on the forces. The ranges for adhesion energy reported in Table 3.2 and shown in Figures 3.6–3.7 are the standard deviations between the four runs.

In the fully hydroxylated pure silica system (Figure 3.3), the range of interaction is about 3.5 Å. The peak forces range from 3.4 to 5.9 nN, and are found at 0.9

and 1.7 Å of separation. The location of the peak will differ depending on which atoms on each surface come into close range first, but there is not much difference between the four cases for this system since the hydroxyl density is high and the surface is fairly homogeneous in terms of both roughness and composition. Some fluctuations in the forces can been seen as the atoms are allowed to adjust to a minimum energy position. This suggests that the results are influenced by the fact that the first 10 Å of bulk atoms, as well as the hydroxyls, are allowed to move. For this system the adhesion energy, found from the minimum in the PMF curves, ranges from 28-45 mJ/m^2.

As the OH density is decreased for the pure silica system (Figures S5 and 3.4), the variation in the peak force and interaction distance grows, and therefore, so does the adhesion energy. This is to be expected since the surfaces become more heterogeneous, and overall are more energetic and have a higher roughness due to the sparseness of the hydroxyl groups. The hydroxyls on one surface are more likely to hydrogen bond with bulk oxygens on the other surface because there is less shielding by hydroxyls. This effect is demonstrated by repeating the adhesion energy calculation on a system where one surface has 3 OH/nm^2 and the other surface has none, such that the average density of the two surfaces together is 1.5 OH/nm^2. The individual force curves are not shown for this system, but the average adhesion energy is just slightly higher than that for the system where both surfaces have 1.5 OH/nm^2 (Figure 3.6), indicating that the hydroxyl groups are essentially shielding the bulk atoms between the two surfaces.

The dry, fully hydroxylated SiO_2 + B_2O_3 system has lower forces and adhesion energy (Figures 3.6 and S6 in Supporting Information) as compared to the pure SiO_2 systems with the same hydroxylation density and amount of water on the

surface. The presence of the B-hydroxyl groups reduces the range of interaction between the slabs, and also lowers the interaction force.

When water is present between the slabs the adhesion depends on the amount of water present. Force and PMF curves are shown in Figure 3.5, and adhesion energies in Figure 3.7 and Table 3.2. The response follows the same trend found in simulations by Leroch et. al. [15] and Cole et. al. [5], and experimentally between silica cracks [33]. Specifically, at low relative humidity the adhesion is at the lowest values, and increases with addition of more water. This effect is also observed in semiconductor wafer bonding, where a small amount of water reduces adhesion, and removing that water by raising the temperature is needed for good adhesion between wafers [10].

The adhesion energies we find for pure silica the values are somewhat lower than those of Leroch, which can be partially attributed to allowing the bulk atoms within 10 Å of the surface to move, but is also a result of the surface-water forcefield. Because the Clay force field over-estimates the water-silica interaction [16] our lower adhesion energies, which are close to those of Cole for systems with water, are reasonable. At saturated conditions, the adhesion energy is approximately equal to the surface tension of water, which has also been seen experimentally for hydrophilic silica spheres [9], and is also in good agreement with the surface energy between hydrophilic silicon surfaces covered by a thin oxide and 1–2 ML of water [10].

At 0.33 ML and above, the mean forces (Figure 3.5) are smooth over the separation distance, and the interaction distance increases with water volume. The smallest amount of water, 0.17 ML, the system exhibits a different behavior, with forces that fluctuate, similar to the dry cases. With higher water volumes a clear

liquid bridge is formed between the plates, with a clear demarcation between water and void space. At 1.5 ML, the shape of the void as the slabs approach each other is cylindrical, with a consistent and low contact angle formed where the water meets each surface. In contrast, with only 0.17 ML of water there are not sufficient molecules for a bridge to form. Rather, the water between surfaces connects as chains of hydrogen bonded molecules, which form and break, resulting in force fluctuations. When the slabs are very close, the forces first become repulsive, but some voids remain where the water has not yet filled in. Some relaxation occurs as the water finds those voids, so the forces again become briefly attractive, until final contact is reached. This behavior is manifested in the two minima in the PMF curve for the 0.17 ML case.

For two of the extreme cases, 0.17 and 1.5 ML of water, the solvent accessible surface area [26] between the slabs was computed over the separation distance, using a solvent size of 1.4 Å. The curves in Figure 3.8 exemplify the different behavior. For the 1.5 ML case, at the longest separation the surface area initially increases and fluctuates as the water reaches out from one side to the other. This is followed by a long steady decrease from about 15 to 5 Å separation, during which time the opening between the slabs remains cylindrical, and the point where the water contacts the surface exhibits a low contact angle which is qualitatively similar to the wetting contact angle observed for a water droplet sitting on the surface (Figure 3.2). Finally the water fills in the open area which drops quickly to full contact. In contrast, the 0.17 ML water case has an open surface area that remains fairly constant down to 5 Å separation, as the water forms chains between the two surfaces but never shows a bridge or wetting angle on the surface. The open area then drops quickly as the surfaces come in full contact. At low RH, capillary forces do not come into play.

Adhesion energies for the SiO_2 + B_2O_3 system with 0.33 and 0.5 ML of water are 10-20% lower than those for the pure silica systems with the same amount of water. The large difference based on composition that we saw for the dry hydroxylated runs is greatly reduced by the presence of water. The same is true for the silica systems with different amounts of hydroxylation, with the largest difference between systems seen with the smallest amount of water, 0.33 ML. The trends in adhesion energy follow the wetting behavior (Figure 3.2) where the surface with the lowest wetting angle has the highest adhesion energy. When the water volume is low the underlying surfaces can still be affected by the opposing surface atoms, but it is expected that at fully saturated conditions there would be little noticeable difference between systems as capillary forces dominate. One surprising result is that the sizable difference in surface wetting and also dry adhesion energies seems to be mostly washed out with the addition of even a small amount of water. Therefore, measuring the contact angle of a surface will not necessarily predict the adhesion energy, particularly for small particles.

3.5 Conclusions

We used molecular dynamics to simulate the conditions of adhesion force measurement in dry and humid conditions, between hydroxylated amorphous plates of pure silica, and also silica plus B_2O_3. The amount of surface hydroxylation was also considered. A non-bonded potential was used to describe the bulk material [22], and DFT energies used to estimate the classical interaction of surface hydroxyls with SPC/E water. While all surfaces considered here are hydrophilic, changes in bulk composition and the surface hydroxyl density change the wetting behavior of water on the surface from fully wetting with 0.7 OH/nm^2 on pure silica, to around

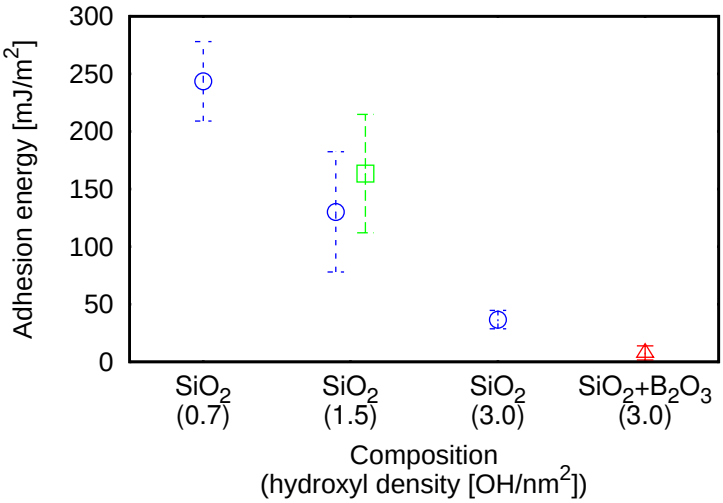

Figure 3.6: Adhesion energies for dry, hydroxylated surfaces. Error bars show the standard deviation between 4 orientations of the top slab around the normal axis. The green square is for the system with all hydroxyls on one surface at 3.0 OH/nm^2 and the other with none, so the average between the two is 1.5 OH/nm^2. All other surfaces have equal hydroxyl density on both.

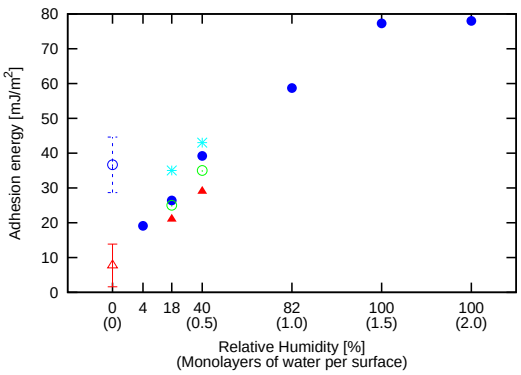

Figure 3.7: Adhesion energies with water. Blue circles: SiO_2, 3 OH/nm^2. Green circles: SiO_2, 1.5 OH/nm^2. Blue stars: SiO_2, 0.7 OH/nm^2. Red triangles: SiO_2 + B_2O_3.

40^o wetting angle on the fully hydroxylated SiO_2 + B_2O_3 slab. The heat of immersion of the pure silica system is about twice that of the SiO_2 + B_2O_3 system. Approximately 1/3 of this difference is due to the difference is the LJ well depth of the two hydroxyl types interacting with water, with the remainder attributed to the effects on the bulk structure induced by the composition change, suggesting

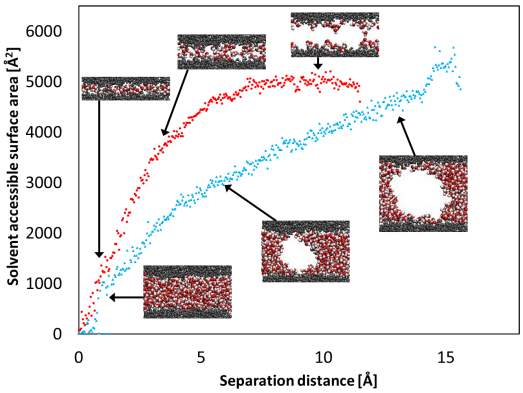

Figure 3.8: Surface area of water throughout adhesion simulations for several silica systems. Filled red circles: 0.17 ML; Open blue triangles: 1.5 ML. Insets: snapshots of water (red and white spheres) between silica slabs (gray spheres) to illustrate key states described in the text.

that the potential describing the underlying bulk material is just as important as the hydroxyl-water interaction.

Adhesion energies were estimated for the two compositions with a fully hydroxylated (3 OH/nm^2) surface, as well as two lower hydroxyl density surfaces for pure silica (1.5 and 0.7 OH/nm^2). Water content ranged from dry (0 ML) to fully saturated (1.5 ML and above) relative humidity conditions.

In dry conditions, the system with B_2O_3 has a much lower adhesion energy because B-hydroxyls at the surface, which have a lower interaction energy than the Si-hydroxyls, play a big role in how the two surfaces interact. The overall hydroxylation density has a larger effect than bulk composition. The directional impact of composition and hydroxyl density is consistent with the wetting behavior described above, but the relative magnitude of adhesion could not be predicted based on wetting contact angle. There is also a significant variability based on alignment of the two dry surfaces as they are brought into contact, which is greater at lower hydroxylation due to the increased heterogeneity of those surfaces.

The difference between the compositions is most pronounced at dry conditions. When a small amount of water is added these differences begin to diminish as the adhesion becomes largely mediated by the water. However, adhesion remains lower in the system with B_2O_3. It is likely that at higher amounts of water the two compositions will have very similar adhesion energy.

For pure silica with < 0.5 ML of water, the adhesion energy goes down compared to the dry case, and then rises to the surface tension of water at saturated conditions (1.5 ML and above). This is consistent with published experimental observations [33, 25]. The two glass compositions show different trends going from dry to low humidity conditions. Whereas the pure silica adhesion is at a minimum at low humidity, the surface with B-hydroxyls is lowest in the dry case. The pure silica surface has higher energy sites which can hydrogen bond with the water, causing some of the water to stay close to the surface rather than to form a liquid bridge with the other surface. The surface with B-hydroxyls does not show this trend because the dry surface is already low energy and is much less likely to hydrogen bond with water.

The simple approach used to estimate the interaction of the surface and water is easily extensible to other species in the Pedone potential, and serves as a path to study adhesion on more complex compositions. For example, one could use DFT calculations to estimate LJ interaction parameters of other oxides, such as CaO or Al_2O_3, with water and then add those oxides to the bulk glass material to estimate their effect on adhesion. There may be additional considerations regarding charges at the surface for network modifiers, such as Ca, Na and K, which we have not addressed here. Also, as the composition becomes more complex the interplay between different types of hydroxyl groups at the surface will be more difficult to

describe with a simple potential, and imposed assumptions about which species will preferentially form hydroxyls may require more rigor.

Another possible extension of our study entails estimating the force that would be needed for the slabs to slide laterally (i.e., as opposed to that for pulling them apart). Generally, when pulling two glass slabs with a force that forms an arbitrary angle with their contacting interface, the force can be decomposed into two orthogonal components: one perpendicular and one parallel to the surface. Just like this study has been concerned with characterizing the "perpendicular" component of that force and its associated adhesion energy, one can also study the parallel component which gives a complementary measure of such adhesion forces that would be more closely associated with the concept of friction. The yield force can be estimated by exerting different trial force values to the upper slab (in a direction parallel to the interface) until the slab yields (starts moving). Our preliminary results indicate that, e.g., for fully hydroxylated pure silica slabs the presence of 0.5ML of interfacial water reduces the yield force by a factor of 100 with respect to the dry case, confirming the expectation that under such conditions water will act as a lubricant.

3.6 Acknowledgments

E. Savoy would like to thank Jim Rustad, Wanda Walczak, Adra Baca, Amy Rovelstad and Gautam Meda, from Corning Incorporated, for invaluable technical discussions and ongoing support of the research.

3.7 Appendix

Additional figures are provided for the distribution of bond valence values, snapshot of water molecule approaching donor Si–hydroxyl, DFT potential energy curves used to fit MD parameters, distribution of hydrogen bonding and angle of hydroxyl with normal for both Si– and B–hydroxyls, and force vs. distance and PMF curves for the 1.5 OH/nm^2 SiO_2 and 3.0 OH/nm^2 SiO_2 + B_2O_3 systems.

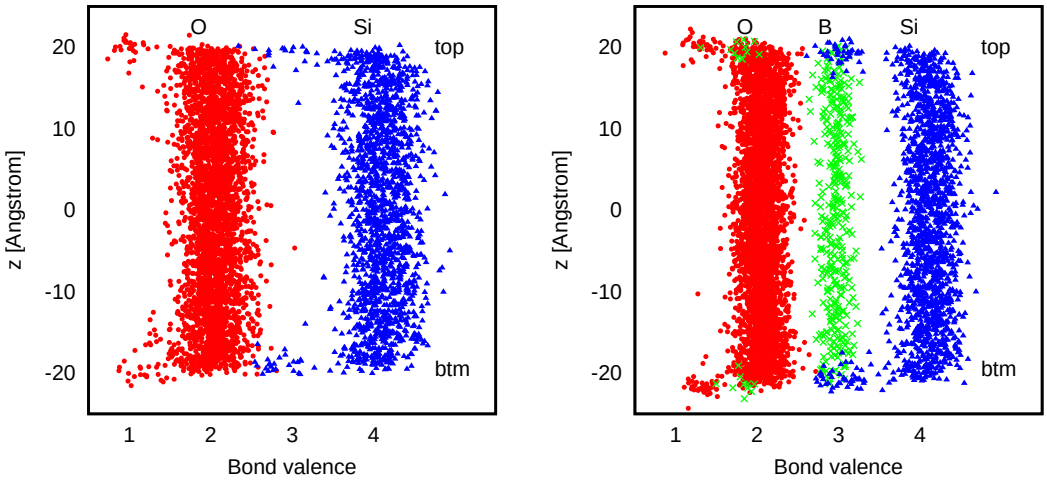

Figure 3.9: Typical bond valence for all O (red circles), Si (blue triangles) and B (green crosses) atoms in the systems as a function of depth in the slab, z. Surfaces exist near $z = \pm 20$ as indicated by "top" and "btm". Left system is pure SiO_2; right is SiO_2 + B_2O_3.

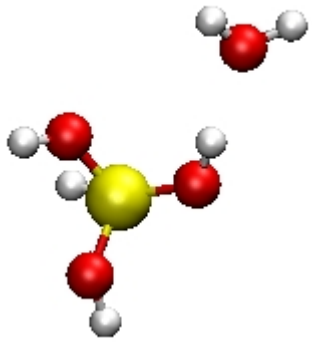

Figure 3.10: Snapshot of single H_4SiO_4 molecule and water molecule used to compute DFT energies for interaction of $O^{h,Si}$ – O^2. yellow: Si; red: O; white: H.

3.7.1 Hydrogen bonding with Si-hydroxyls and B-hydroxyls.

For the SiO_2 + B_2O_3 system with a thick (30 Å) layer of water between slabs, the potential for forming hydrogen bonds between surface hydroxyls and water molecules was evaluated for both types of hydroxyl. For each hydroxyl group, two values were computed: 1) the closest distance to a water molecule, taken as either O_h–H_w or H_h–O_w, and 2) the angle of the hydroxyl from the surface normal, where and angle of 0 means it is pointed out from the surface, perpendicular to the xy plane. The values were averaged over 300 configurations during a post-equilibration run. Histograms of these values (Figure 3.12) show that the Si-hydroxyls get much closer to water molecules and are therefore more likely to form hydrogen bonds. Also most of the hydroxyls of both types are oriented parallel to the surface, with some pointing out of or into the plane of the surface, which is possible due to the molecular scale roughness.

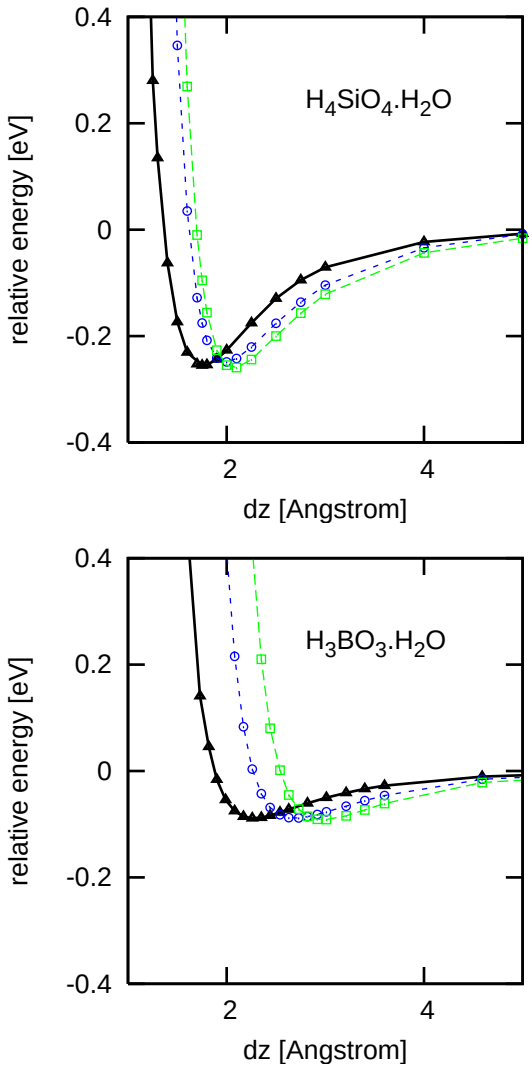

Figure 3.11: Energies of single water molecule approaching a hydroxyl donor from DFT (black triangles) and Classical MD calculations, using two parameters sets: σ=5 (blue circles) and σ=3.5 (green squares)

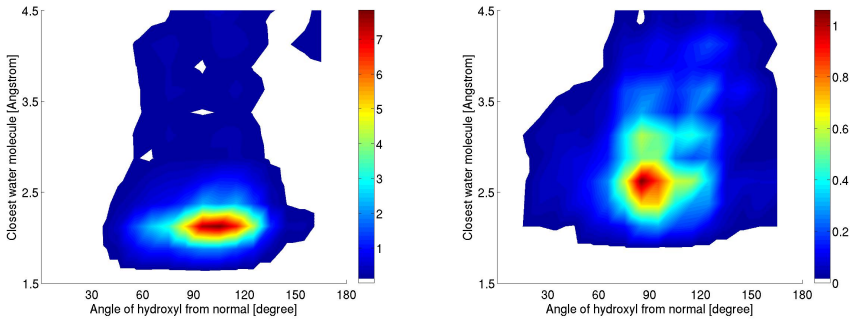

Figure 3.12: Histogram of closest distance from each hydroxyl to a water molecule vs. the angle of the hydroxyl O–H from the surface normal, averaged over 300 post-equilibration configurations. Left: Si–O–H; Right: B–O–H. The color scale is the number of hydroxyls of the given type, where the maximum value corresponds approximately to the total number of hydroxyls of each type at the surface.

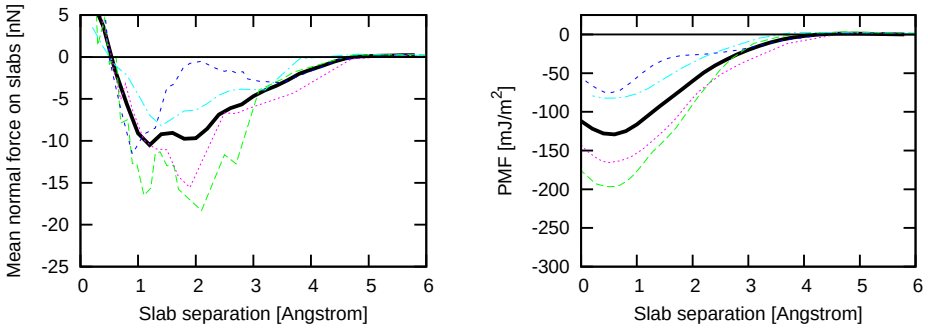

Figure 3.13: Left: Force vs. distance curve for dry hydroxylated (1.5 OH/nm^2) pure silica slabs approaching each other, with four different orientations of the top plate around the normal axis. Right: PMF for the same system. Solid black curve is the average for the four orientations.

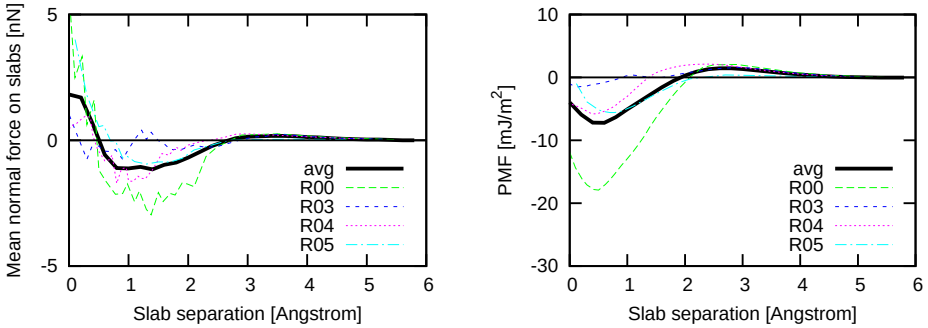

Figure 3.14: Left: Force vs. distance curve for dry hydroxylated (3.0 OH/nm^2) SiO_2 + B_2O_3 slabs approaching each other, with four different orientations of the top plate around the normal axis. Right: PMF for the same system. Solid black curve is the average for the four orientations.

3.7.2 Nomenclature

Symbol	Meaning
b	empirical constant for computing bond valence
D_{ij}, a_{ij} r_0, C_{ij}	tabulated parameters for Pedone potential [22]
$F_{AB}(z)$	mean force acting between plates A and B at the given z separation
r	distance between atom pairs
R_i	distance to all other ions with opposite sign
R_0	nominal bond length
$U(r)$	potential energy of system
v_i	bond valence of each atom i
z_i, z_j	are partial charges on atoms
ϵ	LJ potential well depth
σ	minimum separation distance between atoms in LJ potential
θ	contact angle

Bibliography

[1] Harold D. Ackler, Roger H. French, and Yet-Ming Chiang. Comparisons of hamaker constants for ceramic systems with intervening vacuum or water: From force laws and physical properties. *J. Colloid. Interf. Sci.*, 179:460–469, 1996.

[2] Dimitrios Argyris, Tuan Ho, David R Cole, and Alberto Striolo. Molecular dynamics studies of interfacial water at the alumina surface. *J Phys Chem C*, 115:2038–2046, 2011.

[3] H. J. C. Berendsen, J. R. Grigera, and T. P. Straatsma. The missing term in effective pair potentials. *J. Phys. Chem.*, 91:6269–6271, 1987.

[4] Ian David Brown. Recent developments in the methods and applications of the bond valence model. *Chem. Rev.*, 109:6858–6919, 2009.

[5] Daniel J. Cole, Mike C. Payne, Gábor Csányi, S. Mark Spearing, and Lucio Colombi Ciacchi. Development of a classical force field for the oxidized Si surface: Application to hydrophilic wafer bonding. *J. Chem. Phys.*, 127:204704, 2007.

[6] J. Drelich and Kash L. Mittal, editors. *Atomic Force Microscopy in Adhesion Studies*. Brill Academic Pub, first edition, 2005.

[7] Mahdi Farshchi-Tabrizi, Michael Kappl, Yajun Cheng, Jochen Gutmann, and Hans-Jürgen Butt. On the adhesion between fine particles and nanocontacts: An atomic force microscope study. *Langmuir*, 22:2171–2184, 2006.

[8] Joseph C. Fogarty, Hasan Metin Aktulga, Ananth Y. Grama, Adri C. T. van Duin, and Sagar A. Pandit. A reactive molecular dynamics simulation of the silica-water interface. *J. Chem. Phys.*, 132:174704, 2010.

[9] Masayoshi Fuji, Kotoe Machida, Takashi Takei, Tohru Watanabe, and Masatoshi Chikazawa. Effect of wettability on adhesion force between silica particles evaluated by atomic force microscopy measurement as a function of relative humidity. *Langmuir*, 15:4584–4589, 1999.

[10] U. Gösele and Q.Y. Tong. Semiconductor wafer bonding. *Annual Review of Material Science*, 28:215–241, 1998.

[11] Ali A. Hassanali and Sherwin J. Singer. Model for the water-amorphous silica interface: The undissociated surface. *J. Phys. Chem. B*, 111:11181–11193, 2007.

[12] B. Hess, C. Kutzner, D. van der Spoel, and E. J. Lindahl. Gromacs 4: Algorithms for highly efficient, load-balanced, and scalable molecular simulation. *Chem. Theory Comput.*, 4:435–447, 2008.

[13] T A Ho, D Argyris, D Papavassiliou, A Striolo, L L Lee, and D R Cole. Interfacial water on crystaline silica: A comparative molecular dynamics simulation study. *Mol Simulat*, 37:172–195, 2011.

[14] Jacob N. Israelachvili. *Intermolecular and Surface Forces*. Academic Press, third edition, 2011.

[15] S Leroch and M Wendland. Simulation of forces between humid amorphous silica surfaces: A comparison of empirical atomistic force fields. *J Phys Chem C*, 116:26247–26261, 2012.

[16] Sabine Leroch and Martin Wendland. Influence of capillary bridge formation onto the silica nanoparticle interaction studied by grand canonical monte carlo simulations. *Langmuir*, 29:12410–12420, 2013.

[17] David A. Litton and Stephen H. Garofalini. Modeling of hydrophilic wafer bonding by molecular dynamics simulations. *J. Appl. Phys.*, 89:6013–6023, 2001.

[18] T. S. Mahadevan and S. H. Garofalini. Dissociative chemisorption of water onto silica surfaces and formation of hydronium ions. *J. Phys. Chem. C*, 112:1507–1515, 2008.

[19] A. H. Nazemi and A. Majnooni-Heris. A mathematical model for the interactions between non-identical rough spheres, liquid bridge and liquid vapor. *J. Colloid. Interf. Sci.*, 269:402–410, 2012.

[20] Matti Paajanen, Jukka Katainenh, Olli H. Pakarinen, Adam S. Foster, and Jouko Lahtinen. Experimental humidity dependency of small particle adhesion on silica and titania. *Colloid and Interface Science*, 304:518–523, 2006.

[21] Alfonso Pedone. Properties calculations of silica-based glasses by atomistic simulations techniques: A review. *J. Phys. Chem. C*, 113:20773–20784, 2009.

[22] Alfonso Pedone, Gianluca Malavasi, M. Cristina Menziani, Alastair N. Cormack, and Ulderico Segre. A new self-consistent empirical interatomic potential model for oxides, silicates, and silica-based glasses. *J. Phys. Chem. B*, 110:11780–11795, 2006.

[23] S. Plimpton. Fast parallel algorithms for short-range molecular dynamics (http://lammps.sandia.gov). *Journal of Computational Physics*, 117:1–19, 1995.

[24] Joël Puibasset and Roland J. M. Pellenq. Water adsorption on hydrophilic mesoporous and plane silica substrates: A grand canonical monte carlo simulation study. *J. Chem. Phys.*, 118:5613–5622, 2003.

[25] Yakov I. Rabinovich, Joshua J. Adler, Madhavan S. Esayanur, Ali Ata, Rajiv K. Singh, and Brij M. Moudgil. Capillary forces between surfaces with nanoscale roughness. *Advances in Colloid and Interface Science*, 96:213–230, 2002.

[26] Timothy J. Richmond. Solvent accessible surface area and excluded volume in proteins: Analytical equations for overlapping spheres and implications for the hydrophobic effect. *Journal of Molecular Biology*, 178:63–89, 1984.

[27] James R. Rustad and Benjamin P. Hay. A molecular dynamics study of solvated orthosilicic acid and orthosilicate anion using parameterized potentials. *Geochimica et Cosmochimica Acta*, 59:1251–1257, 1995.

[28] James R. Rustad, Evgeny Wasserman, Andrew R. Felmy, and Chandra Wilke. Molecular dynamics study of proton binding to silica surfaces. *J. Colloid Interface Sci.*, 198:119–129, 1998.

[29] Bertrand Siboulet, Benoît Coasne, Jean-François Dufrêche, and Pierre Turq. Hydrophobic transition in porous amorphous silica. *J. Chem. Phys. B*, 115:7881–7886, 2011.

[30] T. Takei, E. Eriguchi, M. Fuji, T. Watanabe, and M. Chikazawa. Heat of immersion of amorphous and crystalline silicas in water: effect of crystallinity. *Thermochim. Acta*, 308:139–145, 1998.

[31] Adama Tandia, K. Deenamma Vargheese, John C. Mauro, and Arun K. Varshneya. Atomistic understanding of the network dilation anomaly in ion-exchanged glass. *J. Non-Cryst. Sol.*, 358:316–320, 2012.

[32] M. Valiev, E.J. Bylaska, N. Govind, K. Kowalski, T.P. Straatsma, H.J.J. van Dam, D. Wang, J. Nieplocha, E. Apra, T.L. Windus, and W.A. de Jong. Nwchem: a comprehensive and scalable open-source solution for large scale molecular simulations. *Comput. Phys. Commun.*, 181:1477–1489, 2010.

[33] Kai-Tak Wan, Douglas T. Smith, and Brian R. Lawn. Fracture and contact adhesion energies of mica-mica, silica-silica, and mica-silica interfaces in dry and moist atmospheres. *J. Am. Ceram. Soc.*, 75:667–676, 1992.